

# Inverse Models for Estimating the Initial Condition of Spatio-Temporal Advection-Diffusion Processes

Xiao Liu<sup>1</sup> and Kyongmin Yeo<sup>2</sup>

<sup>1</sup>Department of Industrial Engineering, University of Arkansas

<sup>2</sup>IBM T. J. Watson Research Center

## Abstract

Inverse problems involve making inference about unknown parameters of a physical process using observational data. This paper investigates an important class of inverse problems—the estimation of the initial condition of a spatio-temporal advection-diffusion process using spatially sparse data streams. Three spatial sampling schemes are considered, including irregular, non-uniform and shifted uniform sampling. The irregular sampling scheme is the general scenario, while computationally efficient solutions are available in the spectral domain for non-uniform and shifted uniform sampling. For each sampling scheme, the inverse problem is formulated as a regularized convex optimization problem that minimizes the distance between forward model outputs and observations. The optimization problem is solved by the Alternating Direction Method of Multipliers algorithm, which also handles the situation when a linear inequality constraint (e.g., non-negativity) is imposed on the model output. Numerical examples are presented, code is made available on GitHub, and discussions are provided to generate some useful insights of the proposed inverse modeling approaches.

**Key words:** *Inverse Models, Spatio-Temporal Processes, Advection-Diffusion Processes, Alternating Direction Method of Multipliers*

# 1 Introduction

## 1.1 Motivating Examples

Inverse problems involve making inference about unknown parameters of a physical process using observational data, and are widely found in scientific and engineering applications. For example, in urban air quality and environmental monitoring, inverse problems aim at quickly pinpointing the sources of instantaneous emissions of gaseous pollutants that cause public health concerns (Eckhardt et al., 2008; Martinez-Camara et al., 2014; Hwang et al., 2019), or detecting fugitive emissions due to accidental releases from industrial operations (Hosseini and Stockie, 2016; Klein et al., 2016). In healthcare applications, inverse models have been employed to obtain heart-surface potentials from body-surface measurements, known as the inverse ECG problem (Yao and Yang, 2021). In Seismology, inverse problems aim at getting information about the structure of the forces acting in the earthquake’s focus from seismic waves at Earth’s surface (Apostol, 2019). Inverse modeling has also found its applications in detecting the impact location of the missing Malaysian Airlines MH370, using the drift of marine debris (Miron et al., 2019) or acoustic-gravity waves (Kadri, 2019).

This paper investigates an important class of statistical inverse problems—the estimation of the initial condition of a spatio-temporal advection-diffusion process using spatially sparse data streams. Consider the detection of accidental releases of fugitive emissions from industrial operations (Hosseini and Stockie, 2016). Figure 1 shows a  $2 \times 2$  km<sup>2</sup> spatial area that includes a large lead-zinc smelter located in Trail, British Columbia, Canada. The four large red circles indicate the potential emission sources of Zinc Sulphate (ZnSO<sub>4</sub>), while the small blue circles indicate the locations of nine receptors (i.e., sensors) deployed to detect accidental ZnSO<sub>4</sub> leak. The transport of ZnSO<sub>4</sub> is governed by an advection-diffusion equation in the form of a Partial Differential Equation (PDE). In case of accidental ZnSO<sub>4</sub> releases, sensor monitoring data are used to estimate probable emission locations. This inverse prob-

lem requires a statistical model that (i) establish the explicit and interpretable link between observations, emission sources, and process parameters (e.g. wind, diffusivity and decay) by integrating the underlying advection-diffusion physics, (ii) incorporate sensing data streams to estimate the initial condition when  $\text{ZnSO}_4$  is released, and (iii) handle data arising from different sensor network layouts, such as irregular, uniform, non-uniform, nested, etc.

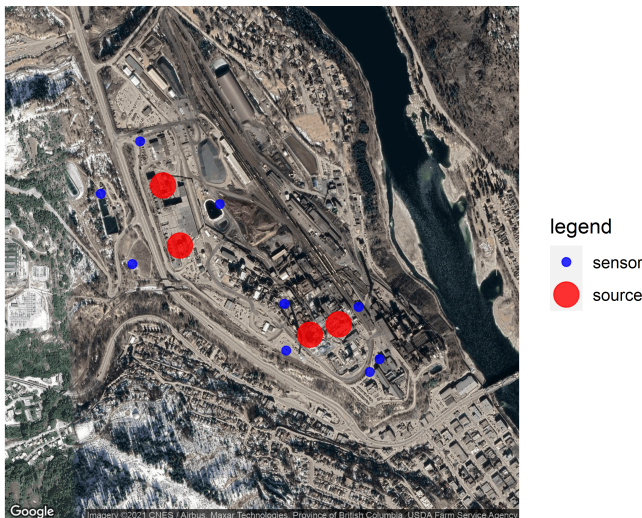


Figure 1: A spatial area that contains four potential  $\text{ZnSO}_4$  emission sources (big red circles) and nine receptors for ground-level measurements (small blue circles)

## 1.2 Statistical Inverse Models and Literature Review

An inverse model typically involves formulating an optimization problem that minimizes the distance between forward model output and observations (Constantinescu et al., 2019). Consider a physical process governed by an equation  $F(\xi, \Theta) = 0$  with  $\xi$  and  $\Theta$  respectively being the state and parameter (unknown). Because the state of the process  $\xi$  must depend on the parameter  $\Theta$  following the governing equation, we may define a mapping from  $\Theta$  to  $\xi$ , i.e.,  $\mathcal{F}(\Theta) = \xi$ , known as the parameter-to-observable map. Once the observations  $\mathbf{Y}$  of the process are available, an inverse problem can be conceptually formulated as  $\hat{\Theta} = \operatorname{argmin}_{\Theta} \mathcal{L}(\mathcal{F}(\Theta), \mathbf{Y})$  where  $\mathcal{L}$  is some pre-defined loss function. For example, Hwang et al. (2019) proposed a Bayesian inverse model to estimate the two-dimensional source functions by exploiting the adjoint advection-diffusion operator. The authors used the finite

difference method to solve both the forward and backward physics models, and constructed the likelihood function for the emission rate given observations. [Oates et al. \(2019\)](#) proposed an inverse model to estimate time-dependent parameters in an electrical potential model for industrial hydrocyclone equipment. Bayesian methods were employed to incorporate statistical models for the errors in the numerical solution of the physical equation. [Yeo et al. \(2019\)](#) proposed a spectral method for source detection of advection-diffusion processes. The authors used the Gaussian radial basis functions to approximate a smooth emission function over space, and the spectral coefficients are modeled by generalized polynomial chaos.

Note that, the physics model  $F$  is typically solved by converting the PDE to a large system of Ordinary Differential Equations (ODE) given a finite difference discretization of the physical domain. When the dimension of the discretization is high, it is often computationally expensive to obtain the forward model output by directly solving the governing equation  $F$ . Statistical surrogate modeling is thus used to construct the parameter-to-observable map  $\mathcal{F}$  ([Mak et al., 2018](#); [Qian et al., 2019](#); [Gul et al., 2018](#)). For example, Gaussian Processes (GP) have been extensively investigated for constructing statistical surrogate models ([Hung et al., 2015](#); [Deng et al., 2017](#); [Gramacy, 2020](#); [Zhang et al., 2021](#); [Sauer et al., 2021](#)). For advection-diffusion processes, in particular, [Sigrist et al. \(2015\)](#) obtained a GP by solving a PDE with an advection-diffusion operator that does not vary in space and time, and [Liu et al. \(2022\)](#) extended this approach by considering spatially-varying advection-diffusion. In recent years, physics-informed machine learning is rapidly emerging for data-driven discovery of governing physics and state/parameter/operator inference which are physically meaningful. For example, [Raissi et al. \(2019\)](#) proposed a deep learning framework for solving both forward and inverse problems for nonlinear partial differential equations. [Chen et al. \(2021\)](#) proposed an active learning approach to estimate the unknown differential equations. An adaptive design criterion combining the D-optimality and the maximin space-filling criterion is used to reduce the experimental data size, where the D-optimality accounts for the unknown

solution of the differential equations and its derivatives.

### 1.3 Problem Statement, Contributions and Overview

In this paper, we investigate a statistical inverse model that aims to estimate the initial condition (over the entire spatial domain) of an advection-diffusion process from spatially sparse sensor measurements. The problem can be formally stated as follows:

**Problem Statement.** *Let  $\xi(t, \mathbf{s})$  be an advection-diffusion process monitored at  $M$  spatial locations for  $L$  discrete time periods, this paper is concerned with an inverse problem that estimates  $\xi(0, \mathbf{s})$  over the entire spatial domain utilizing spatially sparse sensor data streams.*

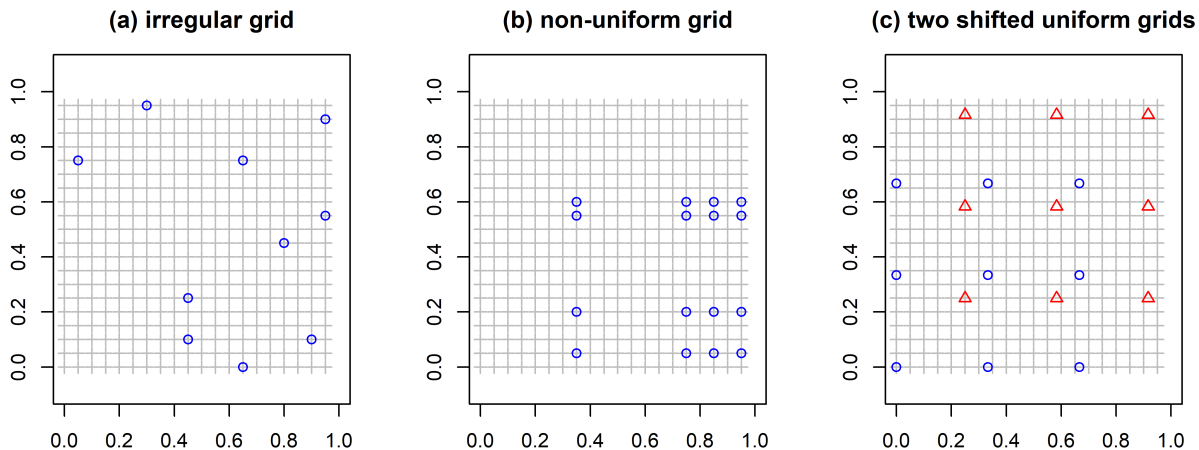


Figure 2: Illustrations of the three spatial sampling schemes considered in this paper: (a) irregular grid, (b) non-uniform grid, and (c) shifted uniform grids (nested).

In particular, three important spatial sampling schemes (i.e., network layout) are considered: *irregular*, *non-uniform*, and *shifted uniform* sampling. Note that, (i) the irregular sampling (Figure 2a) is the general scenario that includes the non-uniform, shifted uniform, and uniform sampling as its special cases; (ii) the two special cases, i.e., non-uniform and shifted uniform sampling (Figures 2b and 2c), are also investigated because computationally efficient solutions are available in the spectral domain for the two special schemes. In practice, non-uniform sampling is often used to minimize acquisition time, sensor installation cost and power consumption, and is particularly useful for monitoring low-activity signals

(Venkataramani and Bresler, 2001; Beyrouthy et al., 2015). Shifted uniform sampling (also known as the nested array or difference co-array) involves two nested uniform sensing networks, and significantly increases the degrees of freedom of linear arrays. By nesting two or more uniform linear arrays, shifted uniform sampling can provide  $\mathcal{O}(M^2)$  degrees of freedom using only  $M$  physical sensors, and thus mitigate the issue of spectral aliasing in spectral analysis (Pal and Vaidyanathan, 2010; Qin and Amin, 2021).

Contributions of this paper are summarized as follows: (i) This paper proposes the first inverse model based on a forward spatio-temporal model for advection-diffusion processes proposed in Liu et al. (2022). This forward model, which provides the parameters-to-observables map  $\mathcal{F}$  for our inverse model, decomposes a physical spatio-temporal process by the linear combination of spatial bases and a multivariate random process of spectral coefficients. The temporal dynamics of spectral coefficients is determined by the advection-diffusion equation so as to integrate the governing physics into statistical models; see Section 2.1. In this paper, following the idea of spectrum decomposition, the estimation of  $\xi(0, \mathbf{s})$  over the entire spatial domain can be performed by estimating the spectral coefficients at time zero that determine  $\xi(0, \mathbf{s})$ . (ii) Because estimating the spectral coefficients at time zero requires sufficient observations over space and time given a sensor network layout, Section 2.2 performs theoretical investigations and obtains sufficient and necessary conditions for the spectral coefficients at time zero to be uniquely estimated. When such conditions are not met, spectral coefficients cannot be uniquely determined and this is known as spectral aliasing in signal processing. (iii) In Section 2.3, we further argue that it is not always possible to uniquely estimate all spectral coefficients at time zero. The sensor network layout and the number of observations in space and time are often subject to practical constraints. Hence, we often require the spectral coefficients to be estimated under the scenarios where neither the sufficient nor necessary conditions are met. It is also noted that, the spectral coefficients may rapidly decay at high-frequency modes if  $\xi(0, \mathbf{s})$  is smooth. To cope with this issue, Section 2.3 presents

a regularized inverse problem that estimates the spectral coefficients at time zero given any irregular sensor network layout. The regularization induces both the sparsity in spectral coefficients and the smoothness of neighboring spectral coefficients. Section 3 presents the special results when data are obtained from non-uniform and shifted uniform sampling, under which computationally efficient solutions are available in the spectral domain. (iv) Finally, Section 4 develops the Alternating Direction Method of Multipliers (ADMM) algorithm for efficiently solving the proposed regularized inverse problem. We then extend the proposed inverse model and the ADMM algorithm to handle non-negativity constraint on  $\xi(0, \mathbf{s})$ , i.e.,  $\xi(0, \mathbf{s}) \geq 0$ . Section 5 provides comprehensive numerical investigations. Sensitivity analysis is performed to demonstrate the robustness of the proposed method.

## 2 Inverse Modeling under General Irregular Sampling

### 2.1 Preliminaries

Consider a physical spatio-temporal advection-diffusion process  $\xi(t, \mathbf{s})$  given by a PDE:

$$\mathcal{A}\xi(t, \mathbf{s}) = \phi(t, \mathbf{s}), \quad \mathbf{s} \in \mathbb{S}, t \geq 0 \quad (1)$$

where  $\mathbb{S}$  is the spatial domain,  $\phi(t, \mathbf{s})$  is the source term, and the advection-diffusion operator  $\mathcal{A}$  is given by  $\mathcal{A}\xi(t, \mathbf{s}) = \dot{\xi}(t, \mathbf{s}) + \vec{\mathbf{v}}^T \nabla \xi(t, \mathbf{s}) - \nabla \cdot [\mathbf{D} \nabla \xi(t, \mathbf{s})] + \zeta \xi(t, \mathbf{s})$  with  $\vec{\mathbf{v}}$ ,  $\mathbf{D}$ ,  $\zeta$ ,  $\nabla$  and  $\nabla \cdot$  respectively being the velocity field, diffusion tensor, decay, gradient and divergence operator. The PDE (1) serves as the governing equation behind an extremely large class of physical phenomena where particles and energy are transferred inside a system.

In this paper, the process  $\xi(t, \mathbf{s})$  can only be observed by spatially distributed sensors at discrete times. Hence, the inverse problem is concerned with estimating the initial condition  $\xi(0, \mathbf{s})$  over the entire spatial domain. Following Liu et al. (2022),  $\xi(0, \mathbf{s})$  is assumed to be spanned by a finite number of orthogonal spatial Fourier basis functions,

$$\xi(0, \mathbf{s}) = \sum_{\mathbf{k} \in \mathcal{K}} \eta(\mathbf{k}) f_{\mathbf{k}}(\mathbf{s}) \quad (2)$$

where  $\mathbf{k} = (k_1, k_2)^T \in \mathcal{K}$  is the wavenumber,  $f_{\mathbf{k}}(\mathbf{s}) = e^{i2\pi\mathbf{s}^T\mathbf{k}}$  is the Fourier basis function,  $\eta(\mathbf{k})$  is the coefficient that determines the weight of each Fourier mode, and

$$\mathcal{K} = \left\{ (k_1, k_2)^T; k_1 = -\frac{N_1}{2} + 1, -\frac{N_1}{2} + 2, \dots, \frac{N_1}{2}, k_2 = -\frac{N_2}{2} + 1, -\frac{N_2}{2} + 2, \dots, \frac{N_2}{2} \right\}. \quad (3)$$

Note that, the equality in (2) holds when the initial condition is band-limited with the high-frequency parts of its Fourier expansion decaying rapidly to exactly zero. Based on (2), it has been shown that the process  $\xi(t, \mathbf{s})$  remains in  $\mathbb{S}$  for  $t \geq 0$  and also admits a spectral representation:  $\xi(t, \mathbf{s}) = \sum_{\mathbf{k} \in \mathcal{K}} \alpha(t, \mathbf{k}) f_{\mathbf{k}}(\mathbf{s})$ , where  $\alpha(t, \mathbf{k})$  is the Fourier coefficient evolving over time, and  $\alpha(0, \mathbf{k}) = \eta(\mathbf{k})$  (Sigrist et al., 2015; Liu et al., 2022).

Next, consider a sensor network with  $M$  sensors at spatial locations  $\mathbf{s}_1, \mathbf{s}_2, \dots, \mathbf{s}_M$ . Let a column vector  $\mathbf{Y}(l) = (Y(l, \mathbf{s}_1), Y(l, \mathbf{s}_2), \dots, Y(l, \mathbf{s}_M))^T$  contain the observations arising from the advection-diffusion process (1) at time  $l$  ( $l = 1, 2, \dots, L$ ), and let a  $M \times L$  matrix  $\mathbf{Y}$  be a collection of the observations from the  $L$  time periods:  $\mathbf{Y} = [\mathbf{Y}(1), \mathbf{Y}(2), \dots, \mathbf{Y}(L)]$ . Then, a spatio-temporal model based on the PDE (1) is proposed in Liu et al. (2022):

$$\mathbf{Y} = \mathbf{F}\mathbf{E}\mathbf{G} + \mathbf{V}. \quad (4)$$

Here,

- $\mathbf{F}$  is an  $M \times N$  matrix of the Fourier basis functions ( $N = N_1 \times N_2$ ),  $\mathbf{F} = (\mathbf{f}_{\mathbf{k}_1}, \mathbf{f}_{\mathbf{k}_2}, \dots, \mathbf{f}_{\mathbf{k}_N})$  where  $\mathbf{f}_{\mathbf{k}_i} = (e^{i2\pi\mathbf{s}_1^T\mathbf{k}_i}, e^{i2\pi\mathbf{s}_2^T\mathbf{k}_i}, \dots, e^{i2\pi\mathbf{s}_M^T\mathbf{k}_i})^T$  and  $i$  is the imaginary unit.

- $\mathbf{E} = \text{diag}(\boldsymbol{\alpha}(0, \mathbf{k})) = \text{diag}(\boldsymbol{\eta})$  is a  $N \times N$  matrix of the spectral coefficients at time 0, and  $\boldsymbol{\eta}$  is a vector that contains  $\eta(\mathbf{k})$  for all  $\mathbf{k} \in \mathcal{K}$ .

- $\mathbf{G}$  is a  $N \times L$  matrix,  $\mathbf{G} = (\mathbf{g}(1), \mathbf{g}(2), \dots, \mathbf{g}(L))$ , which captures the temporal evolution of the elements in  $\mathbf{E}$ . Here,  $\mathbf{g}(l) = (g_1(l), \dots, g_N(l))^T$  is a column vector where  $g_j(l) = e^{\gamma_j(l-1)\Delta}$ ,  $\Delta$  is the sampling interval in time, and  $\gamma_j = -\mathbf{k}_j^T \mathbf{D} \mathbf{k}_j - \zeta - i\bar{\mathbf{v}}^T \mathbf{k}_j$  for  $j = 1, 2, \dots, N$ .

- $\mathbf{V} = (\mathbf{v}(1), \mathbf{v}(2), \dots, \mathbf{v}(L))$  is a  $M \times L$  matrix that captures the measurement error, and  $\mathbf{v}(l)$  is multivariate Gaussian,  $N_M(0, \boldsymbol{\Sigma}_{\mathbf{v}})$ , for  $l = 1, 2, \dots, L$ .

Readers may refer to Sigrist et al. (2015) and Liu et al. (2022) for details of (4). The



model (4) is based on the classical solution of nonlinear dynamical systems using the spectral theory and eigenfunction expansions, and serves as the foundation based on which the inverse models are to be established in this paper.

## 2.2 The Inverse Problem and Its Basic Properties

In an inverse modeling problem considered in this paper,  $\mathbf{Y}$  is the sensor observation, both  $\mathbf{F}$  and  $\mathbf{G}$  are pre-computed, and the goal is to estimate the coefficient vector  $\boldsymbol{\eta}$  that determines the initial condition  $\xi(0, \mathbf{s})$ . Note that, the spectral coefficients  $\boldsymbol{\eta}$  may not be uniquely determined given insufficient observations over space and time and particular sensor network layouts (known as spectral aliasing). Proposition 1 firstly establishes necessary conditions for all components in  $\boldsymbol{\eta}$  to be uniquely estimated.

**Proposition 1.** *Given the observations of the process (1) from  $M$  sensors and for  $L$  discrete time periods, all spectral coefficients in  $\boldsymbol{\eta}$  can be uniquely estimated from the model (4) if at least one of the following two conditions is met:*

*Condition A: given the velocity  $\vec{\mathbf{v}}$  and diffusivity  $\mathbf{D}$ , there exist no  $\mathbf{k}_{j_1}$  and  $\mathbf{k}_{j_2}$  ( $\mathbf{k}_{j_1}, \mathbf{k}_{j_2} \in \mathcal{K}$  and  $j_1 \neq j_2$ ) such that*

$$\vec{\mathbf{v}}^T(\mathbf{k}_{j_1} - \mathbf{k}_{j_2}) = 0 \quad \text{and} \quad \mathbf{k}_{j_1}^T \mathbf{D} \mathbf{k}_{j_1} = \mathbf{k}_{j_2}^T \mathbf{D} \mathbf{k}_{j_2}. \quad (5)$$

*Condition B: There exist at least two sampling locations  $\mathbf{s}$  and  $\mathbf{s}'$  such that neither of the following conditions holds:*

$$2\mathbf{k}_{j_1}(\mathbf{s} - \mathbf{s}') \in \mathbb{Z}^{(odd)}, \quad 2\mathbf{k}_{j_2}(\mathbf{s} - \mathbf{s}') \in \mathbb{Z}^{(odd)} \quad (6a)$$

$$2\mathbf{k}_{j_1}(\mathbf{s} - \mathbf{s}') \in \mathbb{Z}^{(even)}, \quad 2\mathbf{k}_{j_2}(\mathbf{s} - \mathbf{s}') \in \mathbb{Z}^{(even)}. \quad (6b)$$

All proofs are presented in the Supplemental Materials. As shown by this proposition, whether all spectral coefficients in  $\boldsymbol{\eta}$  can be uniquely estimated depends on key physical parameters of the underlying process, such as the velocity  $\vec{\mathbf{v}}$  and diffusivity  $\mathbf{D}$  as one might naturally expect.

Next, we investigate the sufficient condition for all components in  $\boldsymbol{\eta}$  to be uniquely

estimated. In general, the sufficient condition requires either sufficiently large spatial observations (i.e., large  $M$ ), or sufficiently large temporal observations (i.e., large  $L$ ), or both. This is intuitively true and detailed discussions are presented as follows.

**(When the spatial observations are large).** If  $M \geq N$ , the left inverse of  $\mathbf{F}$  exists. Let  $\mathbf{F}_L^{-1}$  be the left inverse of  $\mathbf{F}$ , (4) can be re-written as  $[\mathbf{F}_L^{-1}\mathbf{Y}]^T = \mathbf{G}^T \mathbf{E}^T + [\mathbf{F}_L^{-1}\mathbf{V}]^T$ . Hence, let  $\mathbf{G}_{:,j}^T$  be the  $j$ th column of  $\mathbf{G}^T$ ,  $j = 1, 2, \dots, N$ , we have

$$\text{vec}([\mathbf{F}_L^{-1}\mathbf{Y}]^T) = \text{diag}(\{\mathbf{G}_{:,j}^T\}_{j=1}^N)\boldsymbol{\eta} + \text{vec}([\mathbf{F}_L^{-1}\tilde{\mathbf{V}}]^T) \quad (7)$$

where  $\text{vec}(\cdot)$  denotes matrix vectorization, and  $\text{diag}(\{\mathbf{G}_{:,j}^T\}_{j=1}^N)$  is a block diagonal matrix with the column vector  $\mathbf{G}_{:,j}^T$  being its  $j$ th block. The exponential structure of  $g_{i,j}$  in  $\mathbf{G}$  guarantees that the  $LN \times N$  matrix  $\text{diag}(\{\mathbf{G}_{:,j}^T\}_{j=1}^N)$  is full column rank, and all elements in  $\boldsymbol{\eta}$  can be uniquely determined. Note that, when  $M \geq N$ , the sampling frequency in space exceeds the Nyquist frequency—the largest bandwidth that can be sampled without aliasing.

**(When the temporal observations are large).** A large value of  $L$  corresponds to another scenario where the temporal samples are abundant. By examining the expression of  $\gamma_j$  in (4), it is possible to find  $j$  and  $j'$  ( $j \neq j'$ ) such that  $\gamma_j = \gamma_{j'}$ . In other words, it is possible that  $\mathbf{G}$  is row rank deficient with identical rows.

Let  $\{1, 2, \dots, N\} \xrightarrow{\mathcal{M}} \Psi = \{\Psi_1, \Psi_2, \dots, \Psi_{\tilde{N}}\}$  be a mapping where  $\Psi_i$  ( $i = 1, 2, \dots, \tilde{N}$ ) is a set such that  $\gamma_j = \gamma_{j'}$  for  $j, j' \in \Psi_i$ . In other words, the mapping  $\mathcal{M}$  defines a partition of  $\mathbf{G}$  where each partition contains identical rows, and the row rank of  $\mathbf{G}$  is given by  $\tilde{N}$ .

**Proposition 2.** *If the number of temporal samples  $L$  is greater than the (row) rank of  $\mathbf{G}$ , i.e.,  $L > \tilde{N}$ , the sufficient condition for all components in  $\boldsymbol{\eta}$  to be uniquely determined is*

$$\text{rank}(\tilde{\mathbf{F}}_i) = |\Psi_i|, \quad \forall i = 1, \dots, \tilde{N} \quad (8)$$

where  $\tilde{\mathbf{F}}_i = \{f_{m,j}\}_{m=1, \dots, M, j \in \Psi_i}$  is a  $M \times |\Psi_i|$  matrix, and  $|\Psi_i|$  represents the cardinality of the set  $\Psi_i$  for  $i = 1, \dots, \tilde{N}$ .

## 2.3 A Regularized Inverse Problem

Propositions 1 and 2 above establish sufficient and necessary conditions for all components in  $\boldsymbol{\eta}$  to be uniquely determined from spatially distributed sensor data streams. Despite the theoretical values rooted in the two propositions, real applications may not always require all components in  $\boldsymbol{\eta}$  to be uniquely estimated. For example, the numbers of spatial/temporal samples as well as the locations where sensors can be deployed are always subject to practical constraints. Hence, we often require  $\boldsymbol{\eta}$  to be estimated under the scenarios where neither sufficient nor necessary condition is met.

We first re-write (4) and define  $\vec{\mathcal{Y}}$ ,  $\mathcal{X}^{(P-1)}$ , and  $\vec{\mathcal{V}} \sim N(\mathbf{0}, \boldsymbol{\Sigma})$  as follows:

$$\underbrace{\begin{pmatrix} \mathbf{Y}(1) \\ \vdots \\ \mathbf{Y}(L) \end{pmatrix}}_{\vec{\mathcal{Y}}} = \underbrace{\begin{pmatrix} \mathbf{F} \text{diag}(\{\mathbf{g}_j(1)\}_{j=1}^N) \\ \vdots \\ \mathbf{F} \text{diag}(\{\mathbf{g}_j(L)\}_{j=1}^N) \end{pmatrix}}_{\mathcal{X}^{(P-1)}} \boldsymbol{\eta} + \underbrace{\begin{pmatrix} \mathbf{v}(1) \\ \vdots \\ \mathbf{v}(L) \end{pmatrix}}_{\vec{\mathcal{V}}} \quad (9)$$

and consider a regularized inverse problem:

$$\text{Problem P-I:} \quad \min \frac{1}{2} (\vec{\mathcal{Y}} - \mathcal{X}^{(P-1)} \boldsymbol{\eta})^T \boldsymbol{\Sigma}^{-1} (\vec{\mathcal{Y}} - \mathcal{X}^{(P-1)} \boldsymbol{\eta}) + \mathcal{R}(\boldsymbol{\eta}). \quad (10)$$

Here, the choice of the regularization  $\mathcal{R}(\boldsymbol{\eta})$  is motivated by two considerations: (i) For smooth or band-limited initial condition (see (2)), the high-frequency modes decay rapidly, i.e., the energy is concentrated in the low-frequency region. This motivates us to impose an  $L_1$ -regularization to  $\boldsymbol{\eta}$  (i.e., the *sparsity* of  $\boldsymbol{\eta}$ ). (ii) For smooth initial conditions, it is expected that the components in  $\boldsymbol{\eta}$  gradually decay (not necessarily monotone). This motivates us to impose some level of *smoothness* among the *adjacent* components in  $\boldsymbol{\eta}$  corresponding to adjacent frequencies to prevent sudden spikes of the estimated special coefficients. In particular, an  $L_2$ -regularization is imposed on the difference between the connected components of  $\boldsymbol{\eta}$  in both directions (horizontal and vertical) such that

$$\|\mathbf{J}_1\boldsymbol{\eta}\|_2^2 = \sum_{i,j \in \mathcal{K}^{(h)}} (\eta(\mathbf{k}_i), \eta(\mathbf{k}_j))^2, \quad \|\mathbf{J}_2\boldsymbol{\eta}\|_2^2 = \sum_{i,j \in \mathcal{K}^{(v)}} (\eta(\mathbf{k}_i), \eta(\mathbf{k}_j))^2 \quad (11)$$

where  $\mathbf{J}_1$  and  $\mathbf{J}_2$  are the matrix difference operators in the horizontal and vertical directions, and the set  $\mathcal{K}^{(h)}$  and  $\mathcal{K}^{(v)}$  consist of all frequencies  $\mathbf{k} \in \mathcal{K}$  which are connected in the horizontal and vertical directions, i.e.,  $\mathcal{K}^{(h)} = \{\mathbf{k}_i, \mathbf{k}_j; k_{j,1} - k_{i,1} = 1, i < j\}$  and  $\mathcal{K}^{(v)} = \{\mathbf{k}_i, \mathbf{k}_j; k_{j,2} - k_{i,2} = 1, i < j\}$ . Note that, (11) modifies the idea of Fused Lasso (Tibshirani et al., 2005). The difference is that, Fused Lasso involves an  $L_1$ -regularization to the differences among the coefficients that leads to a sparse and piecewise constant solution, while it is appropriate for us to consider an  $L_2$ -regularization such that the components in  $\boldsymbol{\eta}$  can smoothly change between the high-frequency and low-frequency regions.

Finally, the regularization  $\mathcal{R}(\boldsymbol{\eta})$  in (10) is given by

$$\mathcal{R}(\boldsymbol{\eta}) = \lambda_1 \|\boldsymbol{\eta}\|_1 + \lambda_2 \|\mathbf{J}\boldsymbol{\eta}\|_2^2 \quad (12)$$

where  $\mathbf{J} = (\mathbf{J}_1^T, \mathbf{J}_2^T)^T$  is a 2D difference operator, and  $\lambda_1$  and  $\lambda_2$  respectively control the sparsity in  $\boldsymbol{\eta}$  and the smoothness among the adjacent components in  $\boldsymbol{\eta}$ . The inverse problem (10) can be solved by the Alternating Direction Method of Multipliers (ADMM) (Zou and Hastie, 2005; Ramdas and Tibshirani, 2016). Details of the ADMM algorithm for our problems are provided in Section 4.

### 3 Two Special Cases

In this section, we further investigate two special sampling schemes, i.e., non-uniform sampling and shifted uniform sampling as discussed in Section 2.3, and show that computationally efficient solutions are possible in the spectral domain under the two special schemes.

#### 3.1 Non-Uniform Sampling

Consider a rectangular mesh system given by a tensor product of two one-dimensional collocation sets,  $\tilde{\mathcal{M}} = \tilde{\mathcal{M}}_1 \otimes \tilde{\mathcal{M}}_2$ , where  $\tilde{\mathcal{M}}_1 = \{m_1; m_1 = 0, 1, \dots, \tilde{M}_1 - 1\}$  and  $\tilde{\mathcal{M}}_2 = \{m_2; m_2 = 0, 1, \dots, \tilde{M}_2 - 1\}$  are the sets of collocation points. Here,  $\tilde{\mathcal{M}}$  is a mesh system

consisting of the candidate locations where sensors can potentially be deployed. Let  $\mathcal{M}_1 \subseteq \tilde{\mathcal{M}}_1$  and  $\mathcal{M}_2 \subseteq \tilde{\mathcal{M}}_2$ , a non-uniform sampling grid is given by a mesh system  $\mathcal{M} = \mathcal{M}_1 \otimes \mathcal{M}_2$  where  $|\mathcal{M}_1| = M_1$ ,  $|\mathcal{M}_2| = M_2$ , and  $|\cdot|$  represents the cardinality of a set. Let  $y(l, \mathbf{m})$  represent the observation at time  $l$  and from location  $\mathbf{m} \in \mathcal{M}$ . Then, the non-uniform discrete Fourier transform of type II (NUDFT-II) of  $y(l, \mathbf{m})$  is:

$$\beta(l, \mathbf{q}) = \frac{1}{|\mathcal{M}|} \sum_{\mathbf{m} \in \mathcal{M}} y(l, \mathbf{m}) e^{-i2\pi \mathbf{m}^T \mathbf{q}}, \quad \text{for } \mathbf{q} \in \mathcal{Q}, \quad (13)$$

where  $\mathcal{Q} = \{(q_1, q_2)^T; q_1 = -\frac{M_1}{2} + 1, -\frac{M_1}{2} + 2, \dots, \frac{M_1}{2}, q_2 = -\frac{M_2}{2} + 1, -\frac{M_2}{2} + 2, \dots, \frac{M_2}{2}\}$ .

Replacing  $y(l, \mathbf{m})$  in (13) by its discrete Fourier transform over the domain  $\mathcal{K}$ , we have

$$\begin{aligned} \beta(l, \mathbf{q}) &= \frac{1}{|\mathcal{M}|} \sum_{\mathbf{m}} \left\{ \sum_{\mathbf{k} \in \mathcal{K}} [\alpha(l, \mathbf{k}) + \varepsilon(l, \mathbf{k})] e^{i2\pi \mathbf{m}^T \mathbf{k}} \right\} e^{-i2\pi \mathbf{m}^T \mathbf{q}} \\ &= \sum_{i \in \mathcal{I}_{\mathbf{q}}} \sum_{j \in \mathcal{J}_{\mathbf{q}}} [\alpha(l, \mathbf{q} + (iM_1, jM_2)^T) + \varepsilon(l, \mathbf{q} + (iM_1, jM_2)^T)] \end{aligned} \quad (14)$$

where  $\varepsilon$  is due to the observation error, and the sets  $\mathcal{I}_{\mathbf{q}}$  and  $\mathcal{J}_{\mathbf{q}}$  are respectively given by

$$\begin{aligned} \mathcal{I}_{\mathbf{q}} &= \left\{ i; -\frac{N_1}{2} + 1 \leq (q_1 + iM_1) \leq \frac{N_1}{2}, i \in \mathbb{Z} \right\} \\ \mathcal{J}_{\mathbf{q}} &= \left\{ j; -\frac{N_2}{2} + 1 \leq (q_2 + jM_2) \leq \frac{N_2}{2}, j \in \mathbb{Z} \right\}. \end{aligned} \quad (15)$$

Here, the first line of (14) is obtained by directly inserting the Fourier transform of  $y(l, \mathbf{m})$  into (13). The second line of (14) is obtained by invoking the well-known orthogonal properties of Fourier bases, i.e.,  $\sum_{\mathbf{k} \in \mathcal{K}} [\alpha(l, \mathbf{k}) + \varepsilon(l, \mathbf{k})] e^{i2\pi \mathbf{m}^T (\mathbf{k} - \mathbf{q})} = 1$  only when  $\mathbf{k} = \mathbf{q} + (iM_1, jM_2)^T$  where  $i \in \mathcal{I}_{\mathbf{q}}$  and  $j \in \mathcal{J}_{\mathbf{q}}$ ; otherwise  $\sum_{\mathbf{k} \in \mathcal{K}} [\alpha(l, \mathbf{k}) + \varepsilon(l, \mathbf{k})] e^{i2\pi \mathbf{m}^T (\mathbf{k} - \mathbf{q})} = 0$ . Hence, given a mesh system  $\mathcal{M}$  (i.e., the spatial locations where data are collected), (14) implies that  $\beta(l, \mathbf{q})$  is given by the sum of multiple Fourier coefficients  $\alpha(l, \mathbf{q} + (iM_1, jM_2)^T)$  where  $i \in \mathcal{I}_{\mathbf{q}}$  and  $j \in \mathcal{J}_{\mathbf{q}}$ . In other words, it is not possible to uniquely estimate  $\alpha(l, \mathbf{q} + (iM_1, jM_2)^T)$  for all  $i \in \mathcal{I}_{\mathbf{q}}$  and  $j \in \mathcal{J}_{\mathbf{q}}$  from  $\beta(l, \mathbf{q})$ . This is known as *spectral aliasing*.

To reveal the spectral aliasing structure clearly, we introduce a set  $\mathcal{K}_{\mathbf{q}}$

$$\mathcal{K}_{\mathbf{q}} = \{(k_1, k_2)^T; k_1 = q_1 + iM_1, k_2 = q_2 + jM_2, i \in \mathcal{I}_{\mathbf{q}}, j \in \mathcal{J}_{\mathbf{q}}\} \quad (16)$$

that consists of all wavenumbers in  $\mathcal{K}$  corresponding to  $\mathbf{q} \in \mathcal{Q}$ . Obviously, the Fourier coefficients corresponding to wavenumbers in  $\mathcal{K}_{\mathbf{q}}$  are all confounded, and cannot be uniquely determined unless the number of temporal observations  $L$  is sufficient (see Proposition 2). Consider a simple illustrative example where  $N_1 = N_2 = 4$  and  $M_1 = M_2 = 2$ , and define four sets:  $\mathcal{K}_{(0,0)^T} = \{(0, 0)^T, (0, 2)^T, (2, 0)^T, (2, 2)^T\}$ ,  $\mathcal{K}_{(0,1)^T} = \{(0, 1)^T, (0, -1)^T, (2, 1)^T, (2, -1)^T\}$ ,  $\mathcal{K}_{(1,0)^T} = \{(1, 0)^T, (-1, 0)^T, (1, 2)^T, (-1, 2)^T\}$  and  $\mathcal{K}_{(1,1)^T} = \{(1, 1)^T, (-1, -1)^T, (-1, 1)^T, (1, -1)^T\}$  such that each set consists of the wavenumbers in  $\mathcal{K}$  whose corresponding Fourier coefficients are confounded when the number of temporal samples is insufficient. Note that,  $\bigcup \mathcal{K}_{\mathbf{q}} = \mathcal{K}$  and  $\mathcal{K}_{\mathbf{q}} \cap \mathcal{K}_{\mathbf{q}'} = \emptyset$  for  $\mathbf{q} \neq \mathbf{q}'$ , i.e.,  $\mathcal{K}_{\mathbf{q}}$  are mutually exclusive and exhaustive.

Substituting the temporal dynamics of  $\boldsymbol{\alpha}$  in (4) into (14), we obtain

$$\beta(l, \mathbf{q}) = \mathbf{1}^T \text{diag}(\boldsymbol{\eta}_{\mathbf{q}}) \mathbf{g}_{\mathbf{q}}(l) + \mathbf{1}^T \boldsymbol{\varepsilon}_{\mathbf{q}}(l), \quad l = 1, 2, \dots, L, \quad (17)$$

where  $\mathbf{1}$  is a column vector of ones,  $\mathbf{g}_{\mathbf{q}}(l)$ ,  $\boldsymbol{\varepsilon}_{\mathbf{q}}(l)$  and  $\boldsymbol{\eta}_{\mathbf{q}}$  are respectively the column vectors obtained from  $\mathbf{g}(l)$ ,  $\boldsymbol{\varepsilon}(l)$  and  $\boldsymbol{\eta}$  by keeping only the components corresponding to  $\mathbf{k} \in \mathcal{K}_{\mathbf{q}}$ .

Combining  $\beta(l, \mathbf{q})$  from all  $L$  sampling times, it follows from (17) that

$$\underbrace{\begin{pmatrix} \beta(1, \mathbf{q}) \\ \vdots \\ \beta(L, \mathbf{q}) \end{pmatrix}}_{\boldsymbol{\beta}_{\mathbf{q}}} = \underbrace{\begin{pmatrix} \mathbf{1}^T & & \\ & \ddots & \\ & & \mathbf{1}^T \end{pmatrix}}_{\mathbf{B}_{\mathbf{q}}} \underbrace{\begin{pmatrix} \text{diag}(\mathbf{g}_{\mathbf{q}}(1)) \\ \vdots \\ \text{diag}(\mathbf{g}_{\mathbf{q}}(L)) \end{pmatrix}}_{\mathbf{G}_{\mathbf{q}}} \boldsymbol{\eta}_{\mathbf{q}} + \underbrace{\begin{pmatrix} \mathbf{1}^T & & \\ & \ddots & \\ & & \mathbf{1}^T \end{pmatrix}}_{\mathbf{B}_{\mathbf{q}}} \underbrace{\begin{pmatrix} \boldsymbol{\varepsilon}_{\mathbf{q}}(1) \\ \vdots \\ \boldsymbol{\varepsilon}_{\mathbf{q}}(L) \end{pmatrix}}_{\mathbf{W}_{\mathbf{q}}} \quad (18)$$

where  $\boldsymbol{\beta}_{\mathbf{q}}$  is a  $L \times 1$  column vector,  $\mathbf{B}_{\mathbf{q}} = \text{diag}\{\mathbf{1}^T\}$  is a  $L \times (L \times d_{\mathbf{q}})$  block diagonal matrix with  $d_{\mathbf{q}} = |\mathcal{K}_{\mathbf{q}}|$ , and  $\mathbf{G}_{\mathbf{q}}$  is a  $(L \times d_{\mathbf{q}}) \times d_{\mathbf{q}}$  matrix. Hence, for any  $\mathbf{q} \in \mathcal{Q}$ , we obtain from (17) a linear model

$$\boldsymbol{\beta}_{\mathbf{q}} = \mathbf{B}_{\mathbf{q}} \mathbf{G}_{\mathbf{q}} \boldsymbol{\eta}_{\mathbf{q}} + \mathbf{B}_{\mathbf{q}} \mathbf{W}_{\mathbf{q}}, \quad \mathbf{B}_{\mathbf{q}} \mathbf{W}_{\mathbf{q}} \sim \mathcal{N}(\mathbf{0}, \sigma^2 d_{\mathbf{q}} \mathbf{I}). \quad (19)$$

Note that, several factors determine if the components in  $\boldsymbol{\eta}_{\mathbf{q}}$  can be uniquely determined from the linear model (19), including the sensor network layout  $\mathcal{M}$ , the number of temporal

samples  $L$ , as well as the parameters of the underlying physical process. The following proposition establishes the conditions for the components in  $\boldsymbol{\eta}_{\mathbf{q}}$  to be uniquely estimated.

**Proposition 3.** For  $\mathbf{k}_{j_1}, \mathbf{k}_{j_2} \in \mathcal{K}_{\mathbf{q}}$  and  $j_1 \neq j_2$ , if (i)  $L \geq d_{\mathbf{q}}$ , and (ii) at least one of the conditions,  $\vec{\mathbf{v}}^T(\mathbf{k}_{j_1} - \mathbf{k}_{j_2}) = 0$  and  $\mathbf{k}_{j_1}^T \mathbf{D} \mathbf{k}_{j_1} - \mathbf{k}_{j_2}^T \mathbf{D} \mathbf{k}_{j_2} = 0$ , does not hold, then,  $\mathbf{B}_{\mathbf{q}} \mathbf{G}_{\mathbf{q}}$  is full column rank, and all spectral coefficients in  $\boldsymbol{\eta}_{\mathbf{q}}$  can be uniquely estimated from (19).

Although the proposition above suggests that it is possible to estimate  $\boldsymbol{\eta}_{\mathbf{q}}$  from a system of linear models for all  $\mathbf{q} \in \mathcal{Q}$ , directly solving these individual linear models is rarely appropriate for the following reason: the matrix  $\mathbf{B}_{\mathbf{q}} \mathbf{G}_{\mathbf{q}}$  can be easily ill-conditioned or computationally singular when both  $\vec{\mathbf{v}}^T(\mathbf{k}_{j_1} - \mathbf{k}_{j_2})$  and  $\mathbf{k}_{j_1}^T \mathbf{D} \mathbf{k}_{j_1} - \mathbf{k}_{j_2}^T \mathbf{D} \mathbf{k}_{j_2}$  are close to zero. In other words, some columns in  $\mathbf{B}_{\mathbf{q}} \mathbf{G}_{\mathbf{q}}$  can be near identical. Hence, we combine the linear models (19) for all  $\mathbf{q}_1, \mathbf{q}_2, \dots, \mathbf{q}_{|\mathcal{Q}|}$  and obtain

$$\underbrace{\begin{pmatrix} \beta_{\mathbf{q}_1} \\ \vdots \\ \beta_{\mathbf{q}_{|\mathcal{Q}|}} \end{pmatrix}}_{\vec{\mathcal{Y}}^{(\text{P-II})}} = \underbrace{\begin{pmatrix} \mathbf{B}_{\mathbf{q}_1} \mathbf{G}_{\mathbf{q}_1} & & \\ & \ddots & \\ & & \mathbf{B}_{\mathbf{q}_{|\mathcal{Q}|}} \mathbf{G}_{\mathbf{q}_{|\mathcal{Q}|}} \end{pmatrix}}_{\mathcal{X}^{(\text{P-II})}} \underbrace{\begin{pmatrix} \boldsymbol{\eta}_{\mathbf{q}_1} \\ \vdots \\ \boldsymbol{\eta}_{\mathbf{q}_{|\mathcal{Q}|}} \end{pmatrix}}_{\boldsymbol{\eta}} + \underbrace{\begin{pmatrix} \mathbf{B}_{\mathbf{q}_1} \mathbf{W}_{\mathbf{q}_1} \\ \vdots \\ \mathbf{B}_{\mathbf{q}_{|\mathcal{Q}|}} \mathbf{W}_{\mathbf{q}_{|\mathcal{Q}|}} \end{pmatrix}}_{\boldsymbol{\mathcal{Y}}^{(\text{P-II})}} \quad (20)$$

where  $\vec{\mathcal{Y}}^{(\text{P-II})}$  is a  $(|\mathcal{Q}| \times L) \times 1$  column vector,  $\mathcal{X}^{(\text{P-II})}$  is a  $(|\mathcal{Q}| \times L) \times |\mathcal{K}|$  matrix,  $\boldsymbol{\eta}$  is a  $|\mathcal{K}| \times 1$  column vector,  $\boldsymbol{\mathcal{Y}}^{(\text{P-II})} \sim \mathcal{N}(\mathbf{0}, \boldsymbol{\Sigma}^{(\text{P-II})})$  and  $\boldsymbol{\Sigma}^{(\text{P-II})} = \sigma^2 \text{diag}(\{d_{\mathbf{q}_i} \mathbf{I}\}_{i=1}^{|\mathcal{Q}|})$ .

Similar to Problem P-I (10), we again obtain a regularized inverse problem as follows:

$$\text{Problem P-II: } \min \frac{1}{2} (\vec{\mathcal{Y}}^{(\text{P-II})} - \mathcal{X}^{(\text{P-II})} \boldsymbol{\eta})^T (\boldsymbol{\Sigma}^{(\text{P-II})})^{-1} (\vec{\mathcal{Y}}^{(\text{P-II})} - \mathcal{X}^{(\text{P-II})} \boldsymbol{\eta}) + \mathcal{R}(\boldsymbol{\eta}). \quad (21)$$

where  $\mathcal{R}(\boldsymbol{\eta})$  is defined in (12).

## 3.2 Shifted Uniform Sampling

Shifted uniform sensor arrays or platforms consists of two nested rectangular mesh systems (Figure 2c),  $\mathcal{M}^{(1)}$  and  $\mathcal{M}^{(2)}$ , which are respectively defined by the tensor product of two one-dimensional collocation sets:

$$\mathcal{M}^{(1)} = \left(\frac{m_1}{M_1}; m_1 = 0, 1, \dots, M_1 - 1\right) \otimes \left(\frac{m_2}{M_2}; m_2 = 0, 1, \dots, M_2 - 1\right) \quad (22)$$

$$\mathcal{M}^{(2)} = \left(\frac{m_1}{M_1} + \delta_1; m_1 = 0, 1, \dots, M_1 - 1\right) \otimes \left(\frac{m_2}{M_2} + \delta_2; m_2 = 0, 1, \dots, M_2 - 1\right) \quad (23)$$

where  $0 < \delta_1 < M_1^{-1}$  and  $0 < \delta_2 < M_2^{-1}$ , and  $\boldsymbol{\delta} = (\delta_1, \delta_2)^T$  is the spatial shift between the two sensor platforms. Let  $y^{(1)}(l, \mathbf{m})$  represent the observation at time  $l$  and location  $\mathbf{m}$  from  $\mathcal{M}^{(1)}$ , where  $\mathbf{m} = (\frac{m_1}{M_1}, \frac{m_2}{M_2})^T$ . For any  $\mathbf{q} = (q_1, q_2)^T \in \mathcal{Q}$ , the Fourier coefficient at  $\beta^{(1)}(l, \mathbf{q})$  based on the observations from the first mesh system  $\mathcal{M}^{(1)}$  at time  $l$  is:

$$\begin{aligned} \beta^{(1)}(l, \mathbf{q}) &= \frac{1}{M_1 M_2} \sum_{\mathbf{m}} y^{(1)}(l, \mathbf{m}) e^{-i2\pi \mathbf{m}^T \mathbf{q}} = \frac{1}{M_1 M_2} \sum_{\mathbf{m}} \left\{ \sum_{\mathbf{k} \in \mathcal{K}} [\alpha(l, \mathbf{k}) + \varepsilon(l, \mathbf{k})] e^{i2\pi \mathbf{m}^T \mathbf{k}} \right\} e^{-i2\pi \mathbf{m}^T \mathbf{q}} \\ &= \sum_{i \in \mathcal{I}_{\mathbf{q}}} \sum_{j \in \mathcal{J}_{\mathbf{q}}} \left\{ \alpha(l, \mathbf{q} + (iM_1, jM_2)^T) + \varepsilon(l, \mathbf{q} + (iM_1, jM_2)^T) \right\} \end{aligned} \quad (24)$$

where the sets  $\mathcal{I}_{\mathbf{q}}$  and  $\mathcal{J}_{\mathbf{q}}$  are defined in (15).

Because the second mesh system  $\mathcal{M}^{(2)}$  is obtained from the first mesh system  $\mathcal{M}^{(1)}$  given a shift  $\boldsymbol{\delta}$  in space, the Fourier coefficient,  $\beta^{(2)}(l, \mathbf{q})$ , obtained from the data collected from  $\mathcal{M}^{(2)}$ , can be immediately obtained:

$$\beta^{(2)}(l, \mathbf{q}) = \sum_{i \in \mathcal{I}_{\mathbf{q}}} \sum_{j \in \mathcal{J}_{\mathbf{q}}} \left\{ \alpha(l, \mathbf{q} + (iM_1, jM_2)^T) + \varepsilon(l, \mathbf{q} + (iM_1, jM_2)^T) \right\} e^{i2\pi \boldsymbol{\delta}^T (\mathbf{q} + (iM_1, jM_2)^T)} \quad (25)$$

where the last term  $e^{i2\pi \boldsymbol{\delta}^T (\mathbf{q} + (iM_1, jM_2)^T)}$  is due to the spatial shift from  $\mathcal{M}^{(1)}$  to  $\mathcal{M}^{(2)}$ .

Hence, for  $\mathbf{q} \in \mathcal{Q}$ , one may define a set

$$\mathcal{K}_{\mathbf{q}} = \{(k_1, k_2); k_1 = q_1 + iM_1, k_2 = q_2 + jM_2, i \in \mathcal{I}_{\mathbf{q}}, j \in \mathcal{J}_{\mathbf{q}}\}, \quad (26)$$

and for  $\mathbf{k} \in \mathcal{K}_{\mathbf{q}}$ , we have

$$\begin{pmatrix} \beta^{(1)}(l, \mathbf{q}) \\ \beta^{(2)}(l, \mathbf{q}) \end{pmatrix} = \begin{pmatrix} \mathbf{1}^T \\ \mathbf{b}_{\boldsymbol{\delta}, \mathbf{q}}^T \end{pmatrix} \text{diag}(\boldsymbol{\eta}_{\mathbf{q}}) \mathbf{g}_{\mathbf{q}}(l) + \begin{pmatrix} \mathbf{1}^T \\ \mathbf{b}_{\boldsymbol{\delta}, \mathbf{q}}^T \end{pmatrix} \boldsymbol{\varepsilon}_{\mathbf{q}}(l) \quad (27)$$

for  $l = 1, 2, \dots, L$ . Here,  $\mathbf{1}$  and  $\mathbf{b}_{\boldsymbol{\delta}, \mathbf{q}} = \{e^{i2\pi \boldsymbol{\delta}^T (\mathbf{q} + (iM_1, jM_2)^T)}\}_{i \in \mathcal{I}_{\mathbf{q}}, j \in \mathcal{J}_{\mathbf{q}}}$  are column vectors of length  $d_{\mathbf{q}} = |\mathcal{I}_{\mathbf{q}} \otimes \mathcal{J}_{\mathbf{q}}|$ , and  $\mathbf{g}_{\mathbf{q}}(l)$ ,  $\boldsymbol{\varepsilon}_{\mathbf{q}}(l)$ , and  $\boldsymbol{\eta}_{\mathbf{q}}$  are respectively the column vectors obtained



from  $\mathbf{g}(l)$ ,  $\boldsymbol{\varepsilon}(l)$  and  $\boldsymbol{\eta}$  by keeping only the components corresponding to  $\mathbf{k} \in \mathcal{K}_q$ . Similar to the discussions in Section 3.1,  $\mathcal{K}_q$  consists of all wavenumbers in  $\mathcal{K}$  corresponding to  $\mathbf{q}$  which are aliased and cannot be uniquely determined unless the number of temporal observations  $L$  is sufficiently large. Combining  $\beta^{(1)}(l, \mathbf{q})$  and  $\beta^{(2)}(l, \mathbf{q})$  from all sampling times, we have

$$\underbrace{\begin{pmatrix} \beta^{(1)}(1, \mathbf{q}) \\ \beta^{(2)}(1, \mathbf{q}) \\ \vdots \\ \beta^{(1)}(L, \mathbf{q}) \\ \beta^{(2)}(L, \mathbf{q}) \end{pmatrix}}_{\boldsymbol{\beta}_q^{(\text{P-III})}} = \underbrace{\begin{pmatrix} \mathbf{1}^T \\ \mathbf{b}_{\delta, q}^T \\ \ddots \\ \mathbf{1}^T \\ \mathbf{b}_{\delta, q}^T \end{pmatrix}}_{\mathbf{B}_{\delta, q}} \underbrace{\begin{pmatrix} \text{diag}(\mathbf{g}_q(1)) \\ \vdots \\ \text{diag}(\mathbf{g}_q(L)) \end{pmatrix}}_{\mathbf{G}_q} \boldsymbol{\eta}_q + \underbrace{\begin{pmatrix} \mathbf{1}^T \\ \mathbf{b}_{\delta, q}^T \\ \ddots \\ \mathbf{1}^T \\ \mathbf{b}_{\delta, q}^T \end{pmatrix}}_{\mathbf{B}_{\delta, q}} \underbrace{\begin{pmatrix} \boldsymbol{\varepsilon}_q(1) \\ \vdots \\ \boldsymbol{\varepsilon}_q(L) \end{pmatrix}}_{\mathbf{W}_q} \quad (28)$$

where  $\boldsymbol{\beta}_q^{(\text{P-III})}$  is a  $2L \times 1$  column vector,  $\mathbf{B}_{\delta, q} = \text{diag}\{(\mathbf{1}, \mathbf{b}_{\delta, q})^T\}$  is a  $2L \times (L \times d_q)$  block diagonal matrix with  $d_q = |\mathcal{K}_q|$ , and  $\mathbf{G}_q$  is a  $(L \times d_q) \times d_q$  matrix. For any  $\mathbf{q} \in \mathcal{Q}$ , we have

$$\boldsymbol{\beta}_q^{(\text{P-III})} = \mathbf{B}_{\delta, q} \mathbf{G}_q \boldsymbol{\eta}_q + \mathbf{B}_{\delta, q} \mathbf{W}_q \quad (29)$$

where  $\mathbf{B}_{\delta, q} \mathbf{G}_q$  is a  $2L \times d_q$  matrix. Because  $0 < \delta_1 < M_1^{-1}$  and  $0 < \delta_2 < M_2^{-1}$ , the elements in  $\mathbf{b}_{\delta, q}$  are identical, which immediately makes  $2L \geq d_q$  the sufficient condition for  $\mathbf{B}_{\delta, q} \mathbf{G}_q$  to be full column rank, i.e.,

$$L \geq \frac{d_q}{2} \geq \frac{1}{2} \left\lfloor \frac{N_1 - 1}{M_1} + 1 \right\rfloor \left\lfloor \frac{N_2 - 1}{M_2} + 1 \right\rfloor. \quad (30)$$

As discussed in Section 3.1, directly solving the individual linear models in (29) is not an appropriate choice for ill-conditioned problems. Hence, combining the linear models (29) for all  $\mathbf{q}_1, \mathbf{q}_2, \dots, \mathbf{q}_{|\mathcal{Q}|}$ , we have

$$\underbrace{\begin{pmatrix} \boldsymbol{\beta}_{q_1} \\ \vdots \\ \boldsymbol{\beta}_{q_{|\mathcal{Q}|}} \end{pmatrix}}_{\vec{\boldsymbol{\beta}}^{(\text{P-III})}} = \underbrace{\begin{pmatrix} \mathbf{B}_{\delta, q_1} \mathbf{G}_{q_1} & & \\ & \ddots & \\ & & \mathbf{B}_{\delta, q_{|\mathcal{Q}|}} \mathbf{G}_{q_{|\mathcal{Q}|}} \end{pmatrix}}_{\mathcal{X}^{(\text{P-III})}} \underbrace{\begin{pmatrix} \boldsymbol{\eta}_{q_1} \\ \vdots \\ \boldsymbol{\eta}_{q_{|\mathcal{Q}|}} \end{pmatrix}}_{\boldsymbol{\eta}} + \underbrace{\begin{pmatrix} \mathbf{B}_{\delta, q_1} \mathbf{W}_{q_1} \\ \vdots \\ \mathbf{B}_{\delta, q_{|\mathcal{Q}|}} \mathbf{W}_{q_{|\mathcal{Q}|}} \end{pmatrix}}_{\boldsymbol{\gamma}^{(\text{P-III})}} \quad (31)$$

where  $\vec{\mathcal{Y}}^{(\text{P-III})}$  is a  $(2|\mathcal{Q}| \times L) \times 1$  column vector,  $\mathcal{X}^{(\text{P-III})}$  is a  $(2|\mathcal{Q}| \times L) \times |\mathcal{K}|$  matrix,  $\boldsymbol{\eta}$  is a  $|\mathcal{K}| \times 1$  column vector,  $\mathcal{Y}^{(\text{P-III})} \sim \mathcal{N}(\mathbf{0}, \boldsymbol{\Sigma}^{(\text{P-III})})$ ,  $\boldsymbol{\Sigma}^{(\text{P-III})} = \sigma^2 \text{diag}(\{\mathbf{S}_i\}_{i=1}^{|\mathcal{Q}|})$  and  $\mathbf{S}_i = \text{diag}(d_{\mathbf{q}_i} \mathbf{I}, \|\mathbf{b}_{\delta, \mathbf{q}_i}\|_2^2 \mathbf{I})$  for  $i = 1, 2, \dots, |\mathcal{Q}|$ .

Similar to Problem P-II (21), we obtain a regularized inverse problem:

$$\text{Problem P-III: } \min \frac{1}{2} (\vec{\mathcal{Y}}^{(\text{P-III})} - \mathcal{X}^{(\text{P-III})} \boldsymbol{\eta})^T (\boldsymbol{\Sigma}^{(\text{P-III})})^{-1} (\vec{\mathcal{Y}}^{(\text{P-III})} - \mathcal{X}^{(\text{P-III})} \boldsymbol{\eta}) + \mathcal{R}(\boldsymbol{\eta}) \quad (32)$$

where  $\mathcal{R}(\boldsymbol{\eta})$  is defined in (12).

**Remarks.** Problem P-I estimates the special coefficients  $\boldsymbol{\eta}$  by minimizing the squared distance between forward model outputs and observations in the space-time domain, while Problems P-II and P-III estimate the spectral coefficients  $\boldsymbol{\eta}$  by minimizing the squared distance between the spectral coefficients of forward model outputs and that of observations in the spectral domain. For this reason, when we convert the the optimal solution obtained by P-II and P-III from the spectral domain back to the space-time domain through the inverse Fourier transform, the solution is no longer optimal in the least squares sense (i.e., the squared distance between forward model outputs and observations is not minimized in the space-time domain). This is due to the fact that the least squares estimator is not invariant under transformation. If computational cost is not the primary concern, we recommend one to solve the inverse problem in the space-time domain using Problem P-I (10).

## 4 Solving the Problems P-I, P-II and P-III using ADMM

This section provides the algorithm required to solve the inverse problems P-I, P-II and P-III (throughout this section, the superscripts,  $\cdot^{\text{P-I}}$ ,  $\cdot^{\text{P-II}}$  and  $\cdot^{\text{P-III}}$ , are dropped without causing ambiguity). Note that, the dimension of  $\boldsymbol{\eta}$  in these three inverse problems is given by  $|\mathcal{K}| = N_1 \times N_2$ . Hence, even for moderate size of  $N_1$  and  $N_2$ , the dimension of  $\boldsymbol{\eta}$  can be large. The Alternating Direction Method of Multipliers (ADMM) for large-scale optimization problems becomes a sensible choice.

We first convert an unconstrained problem of the general form

$$\min_{\boldsymbol{\eta}} \frac{1}{2}(\vec{\mathcal{Y}} - \mathcal{X}\boldsymbol{\eta})^T \boldsymbol{\Sigma}^{-1}(\vec{\mathcal{Y}} - \mathcal{X}\boldsymbol{\eta}) + \mathcal{R}(\boldsymbol{\eta}) \quad (33)$$

to a constrained problem:

$$\min_{\boldsymbol{\eta}, \boldsymbol{\psi}} f(\boldsymbol{\eta}) + \mathcal{R}(\boldsymbol{\psi}), \quad \text{s.t. } \boldsymbol{\eta} = \boldsymbol{\psi} \quad (34)$$

where  $f(\boldsymbol{\eta}) = \frac{1}{2}(\vec{\mathcal{Y}} - \mathcal{X}\boldsymbol{\eta})^T \boldsymbol{\Sigma}^{-1}(\vec{\mathcal{Y}} - \mathcal{X}\boldsymbol{\eta})$ . For  $\rho > 0$ , the scaled form of the augmented Lagrangian is written as:

$$f(\boldsymbol{\eta}) + \mathcal{R}(\boldsymbol{\psi}) + \frac{\rho}{2} \|\boldsymbol{\eta} - \boldsymbol{\psi} + \mathbf{u}\|_2^2 + \frac{\rho}{2} \|\mathbf{u}\|_2^2. \quad (35)$$

Then, the ADMM solves the constrained problem (34) by repeating the following iterations (Zou and Hastie, 2005; Ramdas and Tibshirani, 2016):

$$\boldsymbol{\eta}^{(i)} = \operatorname{argmin}_{\boldsymbol{\eta}} f(\boldsymbol{\eta}) + \frac{\rho}{2} \|\boldsymbol{\eta} - \boldsymbol{\psi}^{(i-1)} + \mathbf{u}^{(i-1)}\|_2^2 \quad (36a)$$

$$\boldsymbol{\psi}^{(i)} = \operatorname{argmin}_{\boldsymbol{\psi}} \mathcal{R}(\boldsymbol{\psi}) + \frac{\rho}{2} \|\boldsymbol{\eta}^{(i)} - \boldsymbol{\psi} + \mathbf{u}^{(i-1)}\|_2^2 \quad (36b)$$

$$\mathbf{u}^{(i)} = \mathbf{u}^{(i-1)} + \boldsymbol{\eta}^{(i)} - \boldsymbol{\psi}^{(i)} \quad (36c)$$

for  $i = 1, 2, \dots$ . The iterations satisfy: residual convergence (i.e.,  $\boldsymbol{\eta}^{(i)} - \boldsymbol{\psi}^{(i)} \rightarrow 0$  as  $i \rightarrow \infty$ ), objective convergence (i.e.,  $f(\boldsymbol{\eta}^{(i)}) + \mathcal{R}(\boldsymbol{\psi}^{(i)}) \rightarrow f^* + \mathcal{R}^*$  where  $f^*$  and  $\mathcal{R}^*$  are the primal optimal values), and dual convergence (i.e.,  $\mathbf{u}^{(i)} \rightarrow \mathbf{u}^*$  where  $\mathbf{u}^*$  is the dual solution). Algorithm 1 summarizes the ADMM algorithm developed for solving (33). In the Supplemental Materials, we provide technical details of how each step in Algorithm 1 is obtained.

**Remarks.** Although Problems P-I, P-II and P-III can be solved by the ADMM algorithm, it is noted that Problem P-I is formulated in the space-time domain, while Problems P-II and P-III are constructed in the spectral domain. As a result, the design matrix  $\mathcal{X}^{(P-I)}$  in (9) is a dense matrix, while the design matrices  $\mathcal{X}^{(P-II)}$  and  $\mathcal{X}^{(P-III)}$  in (20) and (31) are sparse (block diagonal), making the computation of  $\mathcal{X}^T \boldsymbol{\Sigma}^{-1} \mathcal{X}$ ,  $\mathcal{X}^T \boldsymbol{\Sigma}^{-1}$  and  $\boldsymbol{\Sigma}^{-1} \mathcal{X}$  faster in the ADMM algorithm. In addition, Problems P-II and P-III enable one to truncate the

high-frequency components because each block of  $\mathcal{X}$ , in both (20) and (31), corresponds to a frequency level. This further helps to reduce the computational time and details are provided in the Supplemental Materials.

In many applications, a non-negativity constraint can be added to the output of the inverse model (e.g., the detected emissions or initial conditions need to be non-negative). When a non-negativity constraint is added, the inverse modeling problem (33) becomes:

$$\min_{\boldsymbol{\eta}} \frac{1}{2} (\vec{\mathcal{Y}} - \mathcal{X} \boldsymbol{\eta})^T \boldsymbol{\Sigma}^{-1} (\vec{\mathcal{Y}} - \mathcal{X} \boldsymbol{\eta}) + \mathcal{R}(\boldsymbol{\eta}), \text{ s.t. } \mathcal{X} \boldsymbol{\eta} \geq 0 \quad (37)$$

In the Supplemental Materials, we show that the constrained problem (37) can be efficiently solved by modifying the ADMM algorithm described in Section 4, which expands the applicability of the proposed model for a wider range of problems.

---

**Algorithm 1:** ADMM for solving the Inverse Problems

---

**Data:**  $\vec{\mathcal{Y}}, \mathcal{X}, \vec{\mathcal{V}}, \lambda_1, \lambda_2$

$\boldsymbol{\eta}^{(0)}, \boldsymbol{\psi}^{(0)}, \mathbf{u}^{(0)}, \rho > 0, \omega > 0$  //initialize

$i \leftarrow 1$

**(the outer loop)**

**while** *convergence criterion is not met* **do**

$$\boldsymbol{\eta}^{(i)} \leftarrow (\mathcal{X}^T \boldsymbol{\Sigma}^{-1} \mathcal{X} + \frac{1}{2} \rho \mathbf{I})^{-1} \left\{ \mathcal{X}^T \boldsymbol{\Sigma}^{-1} \vec{\mathcal{Y}} + \rho (\boldsymbol{\psi}^{(i-1)} + \mathbf{u}^{(i-1)}) \right\}$$

**(the inner loop)**

$\tilde{\boldsymbol{\psi}}^{(0)}$  //initialization for the inner loop

$j \leftarrow 1$

**while** *convergence criterion is not met* **do**

$$\tilde{\boldsymbol{\psi}}^{(j)} \leftarrow \frac{\rho}{2\lambda_2} (\mathbf{J}^T \mathbf{J} + \frac{1}{2} (\rho + \omega) \mathbf{I})^{-1} (\boldsymbol{\eta}^{(i)} + \mathbf{u}^{(i-1)} + \omega \boldsymbol{\theta}^{(j-1)} - \omega \mathbf{v}^{(j-1)})$$

$$\boldsymbol{\theta}^{(j)} \leftarrow S_{\lambda_1/\omega}(\tilde{\boldsymbol{\psi}}^{(j)} + \mathbf{v}^{(j-1)}), \mathbf{v}^{(j)} \leftarrow \mathbf{v}^{(j-1)} + \tilde{\boldsymbol{\psi}}^{(j)} - \boldsymbol{\theta}^{(j)}$$

$j \leftarrow j + 1$

$$\boldsymbol{\psi}^{(i)} \leftarrow \tilde{\boldsymbol{\psi}}^{(j)}, \mathbf{u}^{(i)} \leftarrow \mathbf{u}^{(i-1)} + \boldsymbol{\eta}^{(i)} - \boldsymbol{\psi}^{(i)}$$

$i \leftarrow i + 1$

---

## 5 Numerical Examples

This section presents two numerical examples to illustrate the application of the proposed inverse models and generate some useful insights of the approach.

### 5.1 Example I

We first simulate an advection-diffusion process from the PDE (1) on a  $40 \times 40$  rectangular grid. The parameters of the advection-diffusion operator  $\mathcal{A}$  are chosen as:  $\vec{\mathbf{v}} = (0.5 \times 10^{-2}, 0.5 \times 10^{-2})^T$ ,  $\mathbf{D} = \text{diag}\{0.25 \times 10^{-3}\}$  and  $\zeta = 0$ . The initial condition contains three spatially-sparse instantaneous sources given by  $\Phi(t, \mathbf{s}) = \delta(t - 0) \sum_{j=1}^3 \phi_j(\mathbf{s})$ . Here,  $\phi_j(\mathbf{s}) = \phi_0 \exp\{-\frac{\|\mathbf{s} - \mathbf{s}_0^{(j)}\|_2}{0.09}\}$  where  $\phi_0 = 300$ ,  $\mathbf{s}_0^{(1)} = (0.4, 0.2)^T$ ,  $\mathbf{s}_0^{(2)} = (0.2, 0.4)^T$  and  $\mathbf{s}_0^{(3)} = (0.5, 0.5)^T$ .

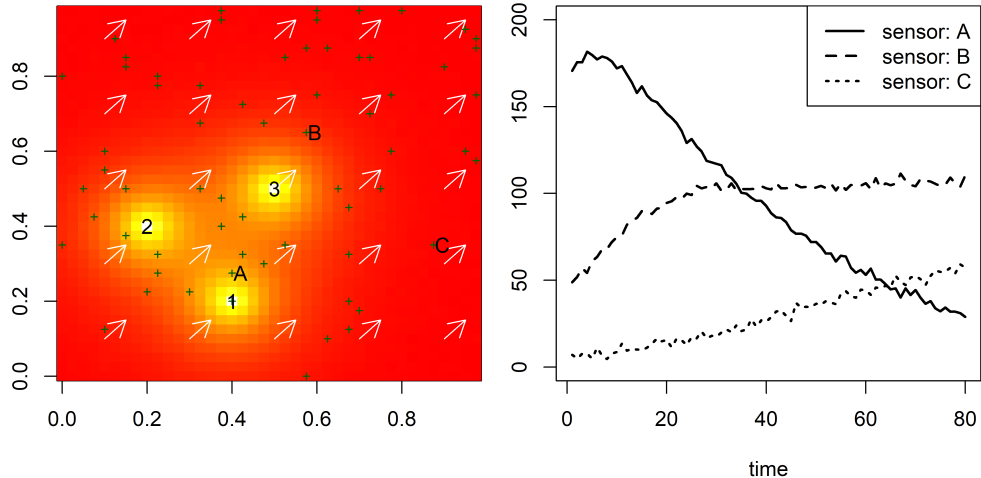


Figure 3: (left panel) the initial condition with three instantaneous sources, velocity field (indicated by white arrows), and locations of 64 randomly distributed sensors; (right panel) noisy sensor measurements over time from three selected sensors, “A”, “B” and “C”.

Figure 3 (left panel) shows the initial condition, velocity field (indicated by arrows), and the locations of 64 randomly distributed sensors (indicated by small crosses). Figure 3 also highlights the locations of three selected sensors, “A”, “B” and “C”, and the measurements over time are shown in the right panel of this figure. The measurement errors are *i.i.d.* samples from a Normal distribution with mean zero and standard deviation two. The strength of the signal from sensor “A” firstly increases when the process (primarily from source 1) quickly reaches location “A”. After that, the signal decreases as the process propagates away

and diffuses. Sensor “B” gradually picks up the signal (firstly from source 3, and then, from the other two sources), while sensor “C” slowly picks up relatively weak signal because this sensor is far from all three sources. The goal is to estimate the initial condition in the absence of the “complete picture” of the spatio-temporal process over the entire spatial domain.

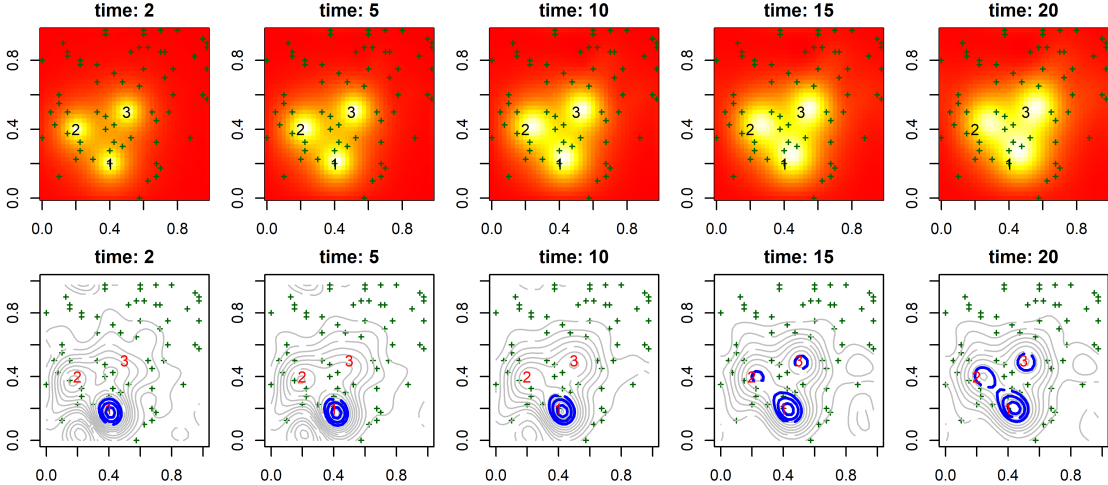


Figure 4: (top row) snapshots of the advection-diffusion process at times 2, 5, 10, 15 and 20; (bottom row) detected spatial sources based on the streaming data from a network of 64 sensors up to times 2, 5, 10, 15 and 20.

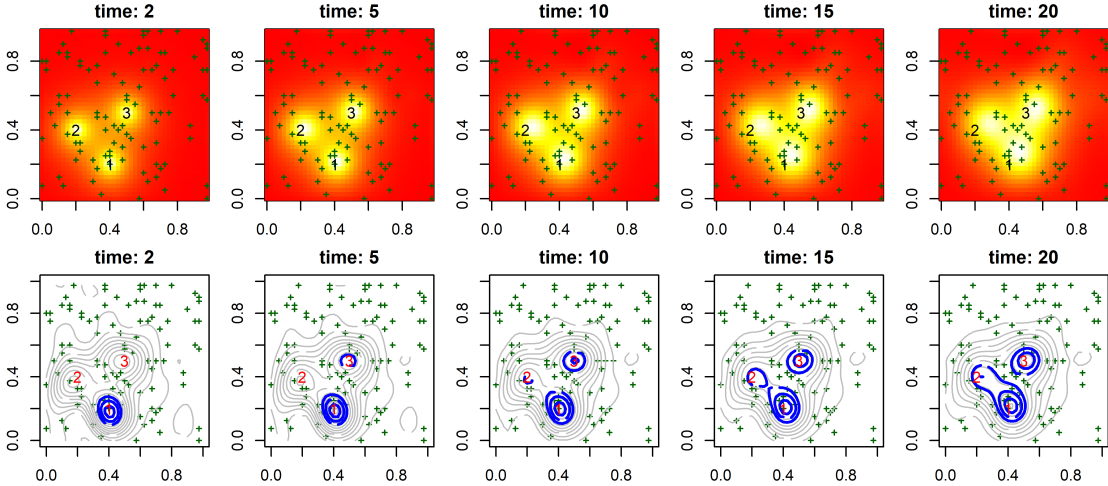


Figure 5: (top row) snapshots of the advection-diffusion process at times 2, 5, 10, 15 and 20; (bottom row) detected spatial sources based on the streaming data from a network of 100 sensors up to times 2, 5, 10, 15 and 20.

The first row of Figure 4 shows the snapshots of the process at times 2, 5, 10, 15 and 20. Solving the Inverse Problem P-I (10) for irregular sampling grid using Algorithm 1, the

second row of Figure 4 shows the contour plots of the estimated initial condition using the sensor observations up to times 2, 5, 10, 15 and 20. The thick blue level sets are respectively the 75th, 85th and 95th percentiles of the output generated by the inverse model. It is seen that, source 1 is quickly detected at time 2. This is only because there happens to be a sensor located near source 1. It is seen that source 2 might also has been detected (circled by a contour line). However, the estimated strength of source 2 is weaker than that of source 1. Source 3 cannot be detected at all at time 2 because most of the sensors have not yet picked up any signal from this source. At time 15, both sources 2 and 3 are clearly detected as the downstream sensors have picked up the signal from these two sources.

Expanding the size of the sensor network is expected to reduce the detection latency. We randomly add another 36 sensors to the existing sensor network (note that, only those sensors added to the downstream areas of the sources may help to reduce the detection latency). Figure 5 presents the updated results: with the additional 36 sensors, all three sources can be detected using the sensor data up to time 10. Figures 4 and 5 well demonstrate the dynamic nature of the inverse problem based on spatially-distributed sensor data streams.

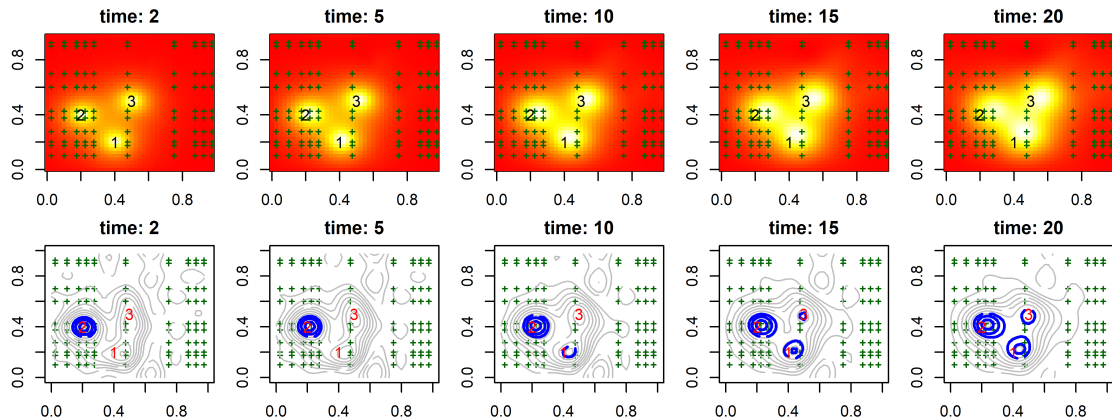


Figure 6: (top row) snapshots of the simulated advection-diffusion process at times 2, 5, 10, 15 and 20; (bottom row) detected spatial sources based on the streaming data from a non-uniform sampling grid up to times 2, 5, 10, 15 and 20.

Next, we investigate the Inverse Problems P-II (21) and P-III (32) for non-uniform sampling grid and shifted sampling grids. Figure 6 shows the output of the Problem P-II based

on the sensor data streams from a non-uniform sampling grid, which is given by a  $10 \times 10$  mesh system generated from a  $40 \times 40$  uniform mesh system as described in Section 3.1. Similar to Figure 4, the first row of Figure 6 shows the snapshots of the process at times 2, 5, 10, 15 and 20, while the second row shows the contour plots of the estimated initial condition using the streaming observations up to times 2, 5, 10, 15 and 20. The thick blue level sets are respectively the 75th, 85th and 95th percentiles of the output generated by the inverse model. We see that, source 2 is almost immediately detected because of its proximity to nearby sensors. Sources 1 and 3 are detected later at times 10 and 15 only when sensors in the downstream areas have picked up the signal originated from these two sources.

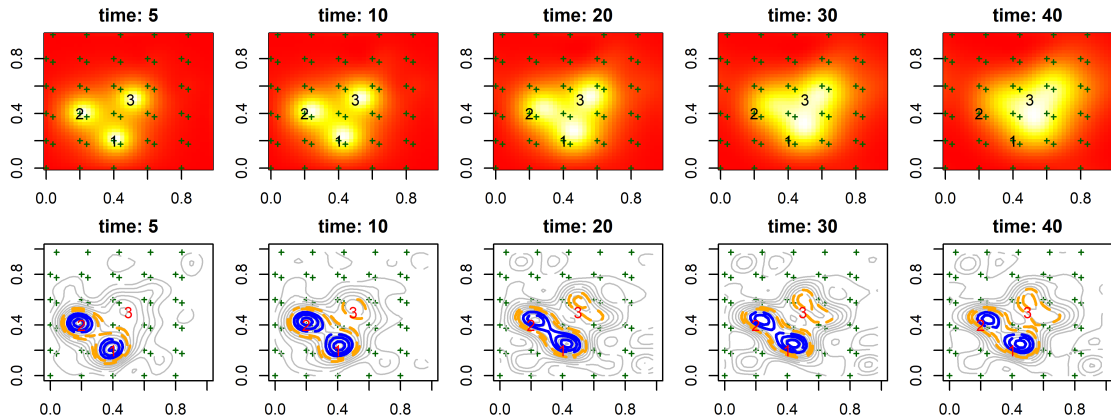


Figure 7: (top row) snapshots of the simulated advection-diffusion process at times 5, 10, 20, 30 and 40; (bottom row) detected spatial sources based on the streaming data from two shifted uniform sampling grids up to times 5, 10, 20, 30 and 40.

Figure 7 shows the dynamic output from the Inverse Problem P-III based on the sensor data streams from two shifted sampling grids. The first sampling grid is a  $5 \times 5$  mesh system, while the second grid is obtained by shifting the first grid by  $\delta = (0.04, 0.175)$ . The first row of Figure 7 shows the process at times 5, 10, 20, 30 and 40, while the second row shows the model output up to times 5, 10, 20, 30 and 40. Similarly, the solid blue thick level sets are respectively the 75th, 85th and 95th percentiles of the output generated by the model, while the dashed thick level sets are the 50th and 60th percentiles of the output generated by the inverse model. We see that, sources 1 and 2 are quickly detected at time 5 because of



their proximity to nearby sensors. Source 3 is detected later when sensors in the downstream areas of source 3 have picked up the signal.

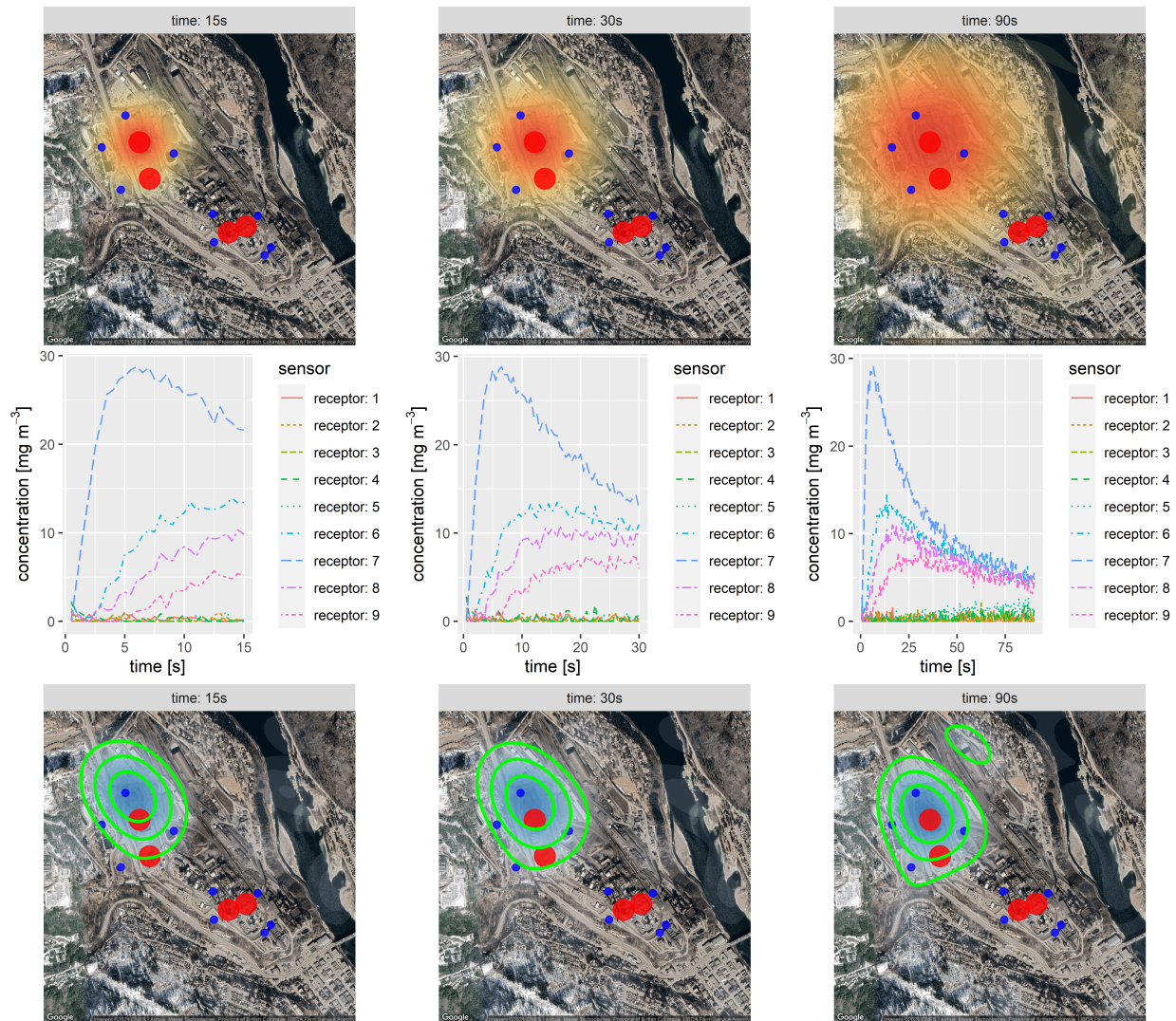


Figure 8: Inverse modeling for a pure diffusion process: (a) concentration of the pollutant 15, 30 and 90 seconds after its release; (b) ground measurements by receptors; (c) contour plots of the output from the inverse model

Example I generates useful insights on the proposed inverse models, and successfully reveals the dynamic nature of the inverse problem using spatially-distributed data streams. A source can be detected when sensors in the downstream areas (if there are any) pick up the signal originated from that source. In the Supplemental Materials, we compare the bias

and Mean-Squared-Error (MSE) of the estimated initial condition  $\hat{\xi}(0, \mathbf{s})$  for different choices of regularizations, including the proposed regularization, generalized Lasso, Elastic Net,  $L_1$  and  $L_2$  regularizations.

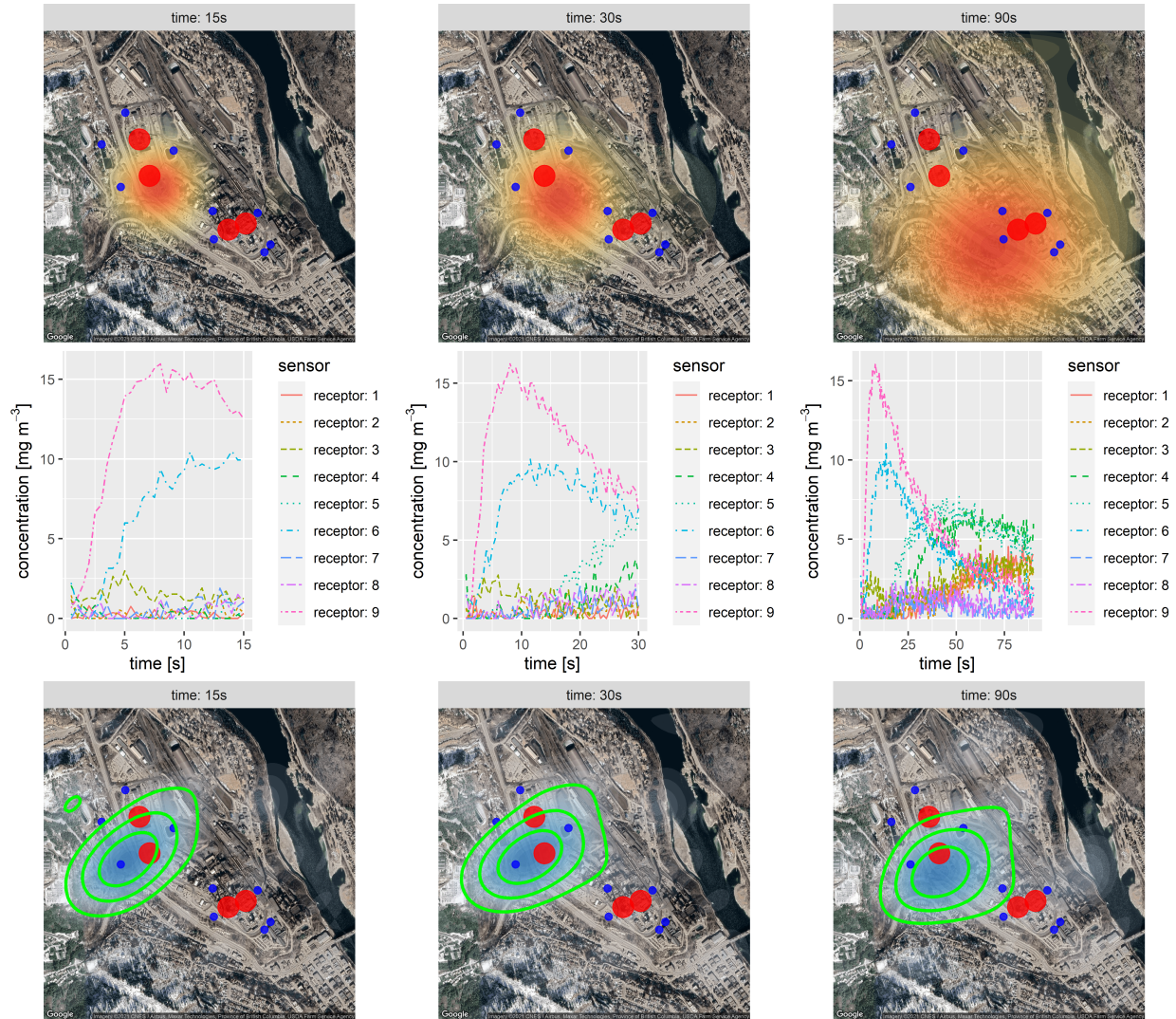


Figure 9: Inverse modeling for an advection-diffusion process: (a) concentration of the pollutant 15, 30 and 90 seconds after its release; (b) ground measurements by receptors; (c) contour plots of the output from the inverse model

## 5.2 Example II

Example II revisits the motivating example described in Section 1.1. This example is concerned with the estimation of emission locations of accidental  $\text{ZnSO}_4$  releases using sensor

monitoring data; see Section 1.1 and Hosseini and Stockie (2016) for more details.

The release and transport of a single contaminant in the atmosphere can be well described by an advection-diffusion equation,  $c(t, \mathbf{s}) + \vec{\mathbf{v}}^T \nabla c(t, \mathbf{s}) - \nabla \cdot [\mathbf{D} \nabla c(t, \mathbf{s})] = \Phi(t, \mathbf{s})$ , where  $c(t, \mathbf{s})$  is the contamination concentration [ $\text{mg m}^{-3}$ ],  $\vec{\mathbf{v}}$  is the wind vector [ $\text{m s}^{-1}$ ],  $\mathbf{D}$  is the diffusivity [ $\text{m}^2 \text{s}^{-1}$ ], and  $\Phi(t, \mathbf{s}) = \delta(t - 0) \sum_{j=1}^4 \phi_j(\mathbf{s})$  is the instantaneous emission source [ $\text{mg m}^{-3} \text{s}^{-1}$ ]. This equation is a special case of the general form (1) in Section 2.

- Scenario 1: pure diffusion. We first consider the scenario where the propagation of  $\text{ZnSO}_4$ , after its release, is driven by a pure diffusion process (i.e., the case when there is no wind). The first row of Figure 8 shows the concentration of the pollutant at times 15, 30 and 90 seconds after its release. As shown by this figure, the pollutant is released from the first source in the north, and propagates to all directions following a pure diffusion process. The second row of Figure 8 shows the noisy measurements over time. The third row of Figure 8 presents the contour plots of the output generated by the inverse model (10) using the streaming observations up to 15, 30 and 90 seconds. As seen in the first and second rows of Figure 8, the sensor located to the north of the source firstly picks up signal. Hence, at times 15 and 30 seconds, the peaks indicated by the contour plot are somewhere between that sensor and the actual source. As more data become available from the other three sensors located near the source (the second row of Figure 8), the peak moves closer to the actual source at time 90 and the emission source is successfully identified. Such observations rationalize the dynamic nature of the proposed inverse problems based on sensor data streams.

- Scenario 2: advection and diffusion. We now consider a more common scenario where the propagation of  $\text{ZnSO}_4$ , after its release, is driven by both advection and diffusion. The pollutant is released from the second source from the top of the spatial domain, and propagates to the southeast direction due to wind. The first row of Figure 9 shows the pollutant concentration at times 15, 30, 90 seconds after its release. The second row shows the noisy

ground-level measurements. The third row of presents the contour plots of the output generated by the inverse model (10) based on the data up to 15, 30 and 90 seconds. As seen in the first and second rows of Figure 9, the sensor located to the west of the source firstly picks up signal. Hence, at times 15 and 30 seconds, the peaks indicated by the contour plot are somewhere between that sensor and the actual source. As more data become available from the other sensors located near the source (shown in the second row of Figure 9), the peak moves closer to the actual source at time 90, accurately pinpointing the source of emission.

- Sensitivity analysis. The accuracy of the input velocity, i.e.,  $\vec{v}$  in the advection-diffusion operator  $\mathcal{A}$ , significantly affects the performance of the inverse model. Imagine that, in the second scenario above, if the specified wind direction is far from the true direction, we no longer expect the model to yield accurate results. Hence, sensitivity analysis is performed to investigate the robustness of the model against the mis-specification of the input velocity and the tuning parameters in the regularization,  $\mathcal{R}$ . Let  $\vec{v} = (v_x, v_y)^T = (10, -10)^T$  be the actual wind vector [ $\text{ms}^{-1}$ ], and let  $\vec{v}^{\text{input}} = (v_x + \epsilon_x^{\text{wind}}, v_y + \epsilon_y^{\text{wind}})^T$  be the input wind vector to the inverse model with random errors,  $\epsilon_x^{\text{wind}} \sim N(0, |v_x|\tau)$  and  $\epsilon_y^{\text{wind}} \sim N(0, |v_y|\tau)$ , i.e., the variance of the error is proportional to the magnitude of the wind vector given a factor  $\tau$ .

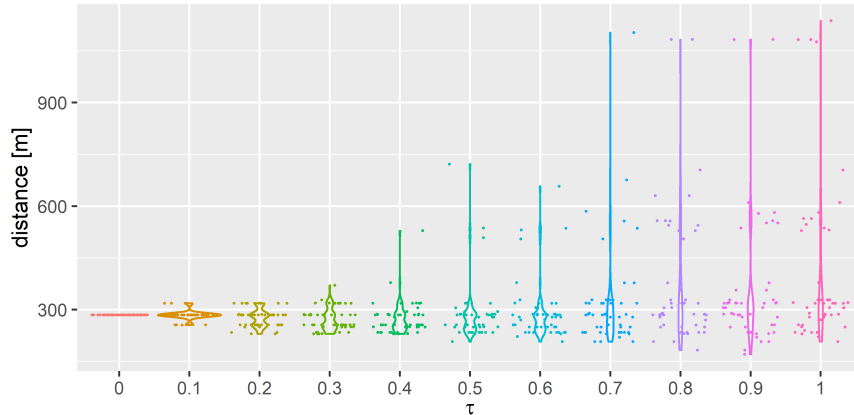


Figure 10: Sensitivity analysis against the mis-specification of input velocity vector.

Consider the second scenario above, Figure 10 shows the violin plot of the distance (in meters) between the detected source and the actual source for different values of  $\tau$  ranging

from 0.1 to 1. For each value of  $\tau$ , the experiment is repeated by 50 times, and a new input wind vector is simulated for each run. It is seen that, the distance between the detected source and the actual source remains within the range from 225m to 380m when  $\tau \leq 0.3$ . In other words, the model performance appears to be robust when the input wind vector does not significantly deviate away from the actual wind vector. In the context of this problem, since the horizontal and vertical components of the actual wind vector are both  $10\text{m s}^{-1}$ , the standard deviation of the random error associated with input wind vector ranges from 1m to 3m in both the horizontal and vertical directions when  $0.1 \leq \tau \leq 0.3$ . Such a margin of specification error is reasonable and can be achieved in many applications where both wind speed and directions are observable (Ding et al., 2021). When  $\tau \geq 0.4$ , we note that the variance of the detection error dramatically increases, indicating a rapid performance deterioration of the inverse model, as expected.

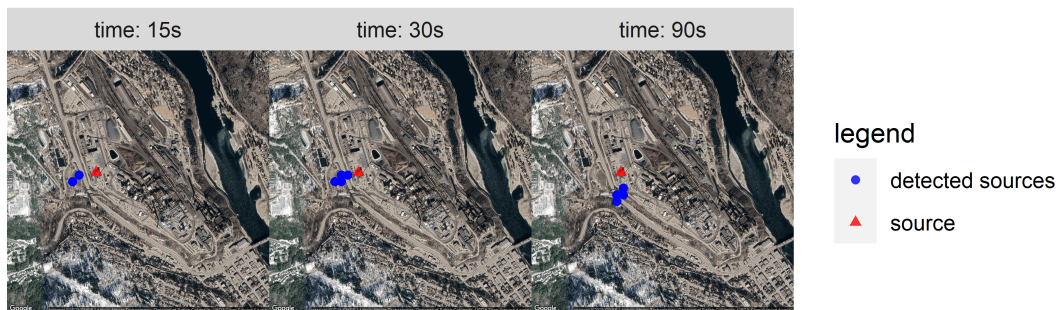


Figure 11: Sensitivity analysis of the detected sources, at times 15, 30 and 90 seconds, for combinations of  $\lambda_1$  and  $\lambda_2$  taken from a mesh grid  $\{5, 10, 15, \dots, 50\} \otimes \{5, 10, 15, \dots, 50\}$ .

The performance of the model also depends on the choice of the tuning parameters,  $\lambda_1$  and  $\lambda_2$ , in the regularization  $\mathcal{R}$ . Note that, for many forward prediction problems, such as Lasso regression, Ridge regression, Elastic Net, etc., the tuning parameters can be chosen through cross-validation. However, the idea of cross-validation no longer applies to inverse problems because the true source is never known and it is impossible to establish the link between the tuning parameters and detection accuracy. Hence, it is more meaningful to investigate the robustness (sensitivity) of the proposed inverse model against  $\lambda_1$  and  $\lambda_2$ . Figure 11 shows the detected sources, at 15, 30 and 90 seconds, for combinations of  $\lambda_1$  and

$\lambda_2$  taken from a mesh grid  $\{5, 10, 15, \dots, 50\} \otimes \{5, 10, 15, \dots, 50\}$ . The figure shows that the detect sources are robust enough against the choices of the tuning parameters parameters. In other words, the true source can be correctly identified for different combinations of  $\lambda_1$  and  $\lambda_2$  chosen from a relatively wide range, which is certainly desirable in practice.

Finally, it is worth noting that if the initial conditions are strictly modeled by delta functions (e.g., “point” sources), the Fourier series of the space-time process does not converge and the proposed approach may generate an oscillatory solution known as the Gibbs phenomenon (Gibbs, 1898). Hence, the proposed approach works well if the initial condition is a smooth function, as seen in the numerical examples above. Even if the initial conditions consist of point sources, the model seeks a solution for a little bit later than the time of release when the point sources become smoother functions due to diffusion.

## 6 Conclusions

Based on a PDE-based statistical model for spatio-temporal data, this paper proposed an inverse modeling approach for advection-diffusion processes utilizing data streams generated by three spatial sampling schemes. The paper obtained both necessary and sufficient conditions under which the Fourier coefficients of the initial condition of the advection-diffusion process can be uniquely estimated. Detailed iteration steps of the ADMM have been obtained, which solves the inverse problems in a computational efficient manner. The algorithm has also been extended for handling a linear inequality constraint on the model output. Numerical examples have been presented to demonstrate the robustness of the proposed inverse models against input model parameters, and reveal the dynamic nature of the inverse problem based on sensor data streams. Note that, the paper considers data arising from a deterministic PDE. One critical future direction is to extend the proposed models for stochastic PDEs, which aim at minimizing the distance between the forward distribution and that of the observations. Computer code is available at <https://github.com/dnncode/inverse-model>.

## Acknowledgments

We are grateful to two reviewers, the Associate Editor and the Editor for their constructive comments, which improved the quality of the paper.

## Funding

This material is based upon work supported by the National Science Foundation under Grant No. 2143695.

## Supplementary Materials

The Supplementary Materials provide (i) the proof of Propositions 1 and 2, (ii) derivation of the ADMM Algorithm 1, (iii) ADMM with non-negativity constraint, (iv) discussions on the computational time of Problems P-I, P-II and P-III, and (v) Numerical comparison on different choices of regularizations.

## References

- Apostol, B. F. (2019), “An inverse problem in seismology: derivation of the seismic source parameters from P and S seismic waves,” *Journal of Seismology*, 23, 1017–1030.
- Beyrouthy, T., Fesquet, L., and Rolland, R. (2015), “Data Sampling and Processing: Uniform vs Non-uniform Schemes,” *2015 International Conference on Event-based Control, Communication, and Signal Processing (EBCCSP)*, DOI: 10.1109/EBCCSP.2015.7300665.
- Chen, J., Kang, L., and Lin, G. (2021), “Gaussian process assisted active learning of physical laws,” *Technometrics*, 63, 329–342.
- Constantinescu, E. M., Petra, N., Bessac, J., and Petra, C. G. (2019), “Statistical Treatment of Inverse Problems Constrained by Differential Equations-Based Models with Stochastic Terms,” *arXiv: 1810.08557v2*.
- Deng, X., Lin, C. D., Liu, K. W., and Rowe, R. K. (2017), “Additive Gaussian Process for Computer Models with Qualitative and Quantitative Factors,” *Technometrics*, 59, 283–292.
- Ding, Y., Kumar, N., Prakash, A., Kio, A., Liu, X., Liu, L., and Li, Q. C. (2021), “A case study of space-time performance comparison of wind turbines on a wind farm,” *Renewable Energy*, 171, 735–746.

- Eckhardt, S., Prata, A. J., Stebel, S. K., and Stohl, A. (2008), “Estimation of the vertical profile of sulfur dioxide injection into the atmosphere by a volcanic eruption using satellite column measurements and inverse transport modeling,” *Atmospheric Chemistry and Physics*, 8, 3881–3897.
- Gibbs, J. W. (1898), “Fourier’s Series,” <https://doi.org/10.1038/059200b0>.
- Gramacy, R. B. (2020), *Surrogates: Gaussian Process Modeling, Design, and Optimization for the Applied Sciences*, Boca Raton, Florida: Chapman & Hall/CRC.
- Gul, E., Joseph, R., Yan, H., and Melkote, S. N. (2018), “Uncertainty Quantification in Machining Simulations Using In Situ Emulator,” *Journal of Quality Technology*, 50, 253–261.
- Hosseini, B. and Stockie, J. M. (2016), “Bayesian estimation of airborne fugitive emissions using a Gaussian plume model,” *Atmospheric Environment*, 141, 122–138.
- Hung, Y., Joseph, R., and Melkote, S. N. (2015), “Analysis of Computer Experiments with Functional Response,” *Technometrics*, 57, 35–44.
- Hwang, Y. D., Kim, H. J., Chang, W., Yeo, K. M., and Kim, Y. (2019), “Bayesian pollution source identification via an inverse physics model,” *Computational Statistics & Data Analysis*, 134, 76–92.
- Kadri, U. (2019), “Effect of sea-bottom elasticity on the propagation of acoustic-gravity waves from impacting objects,” *Scientific Reports*, 9, 912.
- Klein, L. J., Muralidhar, R., Marianno, F. J., Chang, J. B., Lu, S. Y., and Hamann, H. F. (2016), “Geospatial Internet of Things: Framework for fugitive Methane Gas Leaks Monitoring,” in *International Conference on GIScience Short Paper Proceedings*.
- Liu, X., Yeo, K. M., and Lu, S. Y. (2022), “Statistical Modeling for Spatio-Temporal Data from Physical Convection-Diffusion Processes,” *Journal of the American Statistical Association (available on line)*, 117, 1482–1499.
- Mak, S., Sung, C. L., Wang, X., Yeh, S. T., Chang, Y. H., Joseph, R., Yang, V., and Wu, C. F. J. (2018), “An efficient surrogate model of large eddy simulations for design evaluation and physics extraction,” *Journal of the American Statistical Association*, 113, 1443–1456.
- Martinez-Camara, M., Haro, B. B., Stohl, A., and Vetterli, M. (2014), “A robust method for inverse transport modeling of atmospheric emissions using blind outlier detection,” *Geoscientific Model Development*, 7, 2303–2311.
- Miron, P., Beron-Vera, F. J., Olascoaga, M. J., and Koltai, P. (2019), “Markov-chain-inspired search for MH370,” *Chaos*, 29, 041105.
- Oates, C. J., Cockayne, J., Aykroyd, R. G., and Girolami, M. (2019), “Bayesian probabilistic numerical methods in time-dependent state estimation for industrial hydrocyclone equipment,” *Journal of the American Statistical Association*, 114, 1518–1531.
- Pal, P. and Vaidyanathan, P. P. (2010), “Nested Array: A Novel Approach to Array Processing with Enhanced Degrees of Freedom,” *IEEE Transactions on Signal Processing*, 58, 4167–4181.



- Qian, E., Karamer, B., Peherstorfer, B., and Willcox, K. (2019), “Lift & Learn: Physics-informed machine learning for large-scale nonlinear dynamical systems,” *Oden Institute Report 19-18*.
- Qin, G. and Amin, M. G. (2021), “Structured Sparse Array Design Exploiting Two Uniform Subarrays for DOA Estimation on Moving Platform,” *Signal Processing*, 180, 107872.
- Raissi, M., Perdikaris, P., and Karniadakis, G. E. (2019), “Physics-informed neural networks: A deep learning framework for solving forward and inverse problems involving nonlinear partial differential equations,” *Journal of Computational Physics*, 378, 686–707.
- Ramdas, A. and Tibshirani, R. J. (2016), “Fast and Flexible ADMM Algorithms for Trend Filtering,” *Journal of Computational and Graphical Statistics*, 25, 839–858.
- Sauer, A., Gramacy, R. B., and Higdon, D. (2021), “Active Learning for Deep Gaussian Process Surrogates,” *arXiv:2012.08015*.
- Sigrist, F., Kunsch, H. R., and Stahel, W. A. (2015), “Stochastic Partial Differential Equation based Modelling of Large Space-Time Data Sets,” *Journal of the Royal Statistical Society: Series B*, 77, 3–33.
- Tibshirani, R., Rosset, S., Zhu, J., and Knight, K. (2005), “Sparsity and Smoothness via the Fused Lasso,” *Journal of the Royal Statistical Society: Series B (Statistical Methodology)*, 67, 91–108.
- Venkataramani, R. and Bresler, Y. (2001), “Optimal sub-Nyquist nonuniform sampling and reconstruction for multiband signals,” *IEEE Transactions on Signal Processing*, 49, 2301–2313.
- Yao, B. and Yang, H. (2021), “Spatiotemporal regularization for inverse ECG modeling,” *IJSE Transactions on Healthcare Systems Engineering*, 11, 11–23.
- Yeo, K. M., Hwang, Y. D., Liu, X., and Kalagnanam, J. (2019), “Development of hp-inverse model by using generalized polynomial chaos,” *Computer Methods in Applied Mechanics and Engineering*, 347, 1–20.
- Zhang, B. Y., Cole, D. A., and Gramacy, R. B. (2021), “Distance-distributed design for Gaussian process surrogates,” *arXiv:1812.02794*.
- Zou, H. and Hastie, T. (2005), “Regularization and variable selection via the elastic net,” *Journal of the Royal Statistical Society: Series B (Statistical Methodology)*, 67, 301–320.

# Inverse Models for Estimating the Initial Condition of Spatio-Temporal Advection-Diffusion Processes

Xiao Liu

Department of Industrial Engineering, University of Arkansas

Kyongmin Yeo

IBM T. J. Watson Research Center

## Supplemental Materials

### 1. Proof of Proposition 1

*Proof.* To show Proposition 1, note that

- For any  $\mathbf{k}_{j_1}$  and  $\mathbf{k}_{j_2}$  ( $\mathbf{k}_{j_1}, \mathbf{k}_{j_2} \in \mathcal{K}$  and  $j_1 \neq j_2$ ) such that  $\bar{\mathbf{v}}^T(\mathbf{k}_{j_1} - \mathbf{k}_{j_2}) = 0$  and  $\mathbf{k}_{j_1}^T \mathbf{D} \mathbf{k}_{j_1} = \mathbf{k}_{j_2}^T \mathbf{D} \mathbf{k}_{j_2}$ , it is immediately implied by  $\gamma_j = -\mathbf{k}_j^T \mathbf{D} \mathbf{k}_j - \zeta - i \bar{\mathbf{v}}^T \mathbf{k}_j$  that the two vectors  $(g_{j_1}(1), \dots, g_{j_1}(L))$  and  $(g_{j_2}(1), \dots, g_{j_2}(L))$  become identical;

- For a given  $\mathbf{s}$ , the complex exponential  $e^{i2\pi \mathbf{s}^T \mathbf{k}_{j_1}}$  and  $e^{i2\pi \mathbf{s}^T \mathbf{k}_{j_2}}$  are not linearly independent in the complex domain  $\mathbb{C}$ . For example, there exist  $u, v \in \mathbb{R}$  (at least one of them is non-zero) such that  $(u + vi)e^{i2\pi \mathbf{s}^T \mathbf{k}_{j_1}} = (u - vi)e^{i2\pi \mathbf{s}^T \mathbf{k}_{j_2}}$ ;

- For a pair of sampling locations  $\mathbf{s}$  and  $\mathbf{s}'$ , if both  $2\mathbf{k}_{j_1}(\mathbf{s} - \mathbf{s}')$  and  $2\mathbf{k}_{j_2}(\mathbf{s} - \mathbf{s}')$  return even numbers, then,  $e^{i2\pi \mathbf{s}^T \mathbf{k}} = e^{i2\pi \mathbf{s}'^T \mathbf{k}}$ . Similarly, if both  $2\mathbf{k}_{j_1}(\mathbf{s} - \mathbf{s}')$  and  $2\mathbf{k}_{j_2}(\mathbf{s} - \mathbf{s}')$  return odd numbers, then,  $e^{i2\pi \mathbf{s}^T \mathbf{k}} = -e^{i2\pi \mathbf{s}'^T \mathbf{k}}$ .

Hence, the matrix  $\mathcal{X}^{(P-1)}$  in (9) has independent columns if one of the conditions A and B in Proposition 1 holds. When  $ML \geq N$ ,  $\mathcal{X}^{(P-1)}$  has a full column rank of  $N$ , and the condition in Proposition 1 is also sufficient for components in  $\boldsymbol{\eta}$  to be uniquely determined. ■

## 2. proof of Proposition 2

*Proof.* We first construct a new matrix  $\tilde{\mathbf{G}}$  by eliminating the redundant rows (if there is any) in  $\mathbf{G}$  as follows: Let  $\mathbf{g}_{i\cdot}$  be the  $i$ th row  $\mathbf{G}$ . For  $i = 2, \dots, N$ , if there exists  $i' = 1, \dots, i - 1$  such that  $\mathbf{g}_{i\cdot} = \mathbf{g}_{i'\cdot}$ , the row  $\mathbf{g}_{i\cdot}$  is eliminated from  $\mathbf{G}$ . By eliminating the repeated rows from  $\mathbf{G}$ , the matrix  $\tilde{\mathbf{G}}$  is full row rank when  $L \geq \tilde{N}$ .

Let  $\mathbf{H} = (\mathbf{h}_{\cdot,1}, \mathbf{h}_{\cdot,2}, \dots, \mathbf{h}_{\cdot,\tilde{N}})$  be a  $N \times \tilde{N}$  matrix with  $\mathbf{h}_{\cdot,j}$  representing the  $j$ th column vector of  $\mathbf{H}$ . For any column vector  $\mathbf{h}_{\cdot,j}$ , its  $i$ th element  $h_{i,j} = 1$  if  $i \in \Psi_j$ ; otherwise,  $h_{i,j} = 0$ . Then, (4) can be re-written as

$$\mathbf{Y} = \mathbf{F}(\mathbf{E}\mathbf{H})\tilde{\mathbf{G}} + \mathbf{V}. \quad (38)$$

Since  $\tilde{\mathbf{G}}$  is full row rank of  $\tilde{N}$  (when  $L \geq \tilde{N}$ ), we re-write (38) as follows:

$$\mathbf{Y}\tilde{\mathbf{G}}_R^{-1} = \mathbf{F}(\mathbf{E}\mathbf{H}) + \mathbf{V}\tilde{\mathbf{G}}_R^{-1} \quad (39)$$

where  $\tilde{\mathbf{G}}_R^{-1}$  is the right inverse of  $\tilde{\mathbf{G}}$ .

Let  $\mathbf{Y}\tilde{\mathbf{G}}_R^{-1} \equiv \tilde{\mathbf{Y}} = (\tilde{\mathbf{Y}}_1, \tilde{\mathbf{Y}}_2, \dots, \tilde{\mathbf{Y}}_{\tilde{N}})$ ,  $\tilde{\mathbf{F}}_i = \{f_{m,j}\}_{m=1,\dots,M,j \in \Psi_i}$  be a  $M \times |\Psi_i|$  matrix, and  $\mathbf{V}\tilde{\mathbf{G}}_R^{-1} \equiv \tilde{\mathbf{\Omega}} = (\tilde{\mathbf{\Omega}}_1, \tilde{\mathbf{\Omega}}_2, \dots, \tilde{\mathbf{\Omega}}_{\tilde{N}})$ . Then, (39) defines a system of  $\tilde{N}$  linear models

$$\tilde{\mathbf{Y}}_i = \tilde{\mathbf{F}}_i \boldsymbol{\eta}_i + \tilde{\mathbf{\Omega}}_i, \quad \forall i = 1, 2, \dots, \tilde{N} \quad (40)$$

where  $\boldsymbol{\eta}_i$  is a column vector  $\{\eta(\mathbf{k}_j)\}_{j \in \Psi_i}$ . Hence, the sufficient condition for all components in  $\boldsymbol{\eta}$  to be uniquely determined is  $\text{rank}(\tilde{\mathbf{F}}_i) = |\Psi_i|$  for all  $i = 1, \dots, \tilde{N}$  ■.

## 3. derivation of the ADMM Algorithm 1

The ADMM solves the constrained problem (34) by repeating the following iterations (Zou and Hastie, 2005; Ramdas and Tibshirani, 2016):

$$\boldsymbol{\eta}^{(i)} = \operatorname{argmin}_{\boldsymbol{\eta}} f(\boldsymbol{\eta}) + \frac{\rho}{2} \|\boldsymbol{\eta} - \boldsymbol{\psi}^{(i-1)} + \mathbf{u}^{(i-1)}\|_2^2 \quad (41a)$$

$$\boldsymbol{\psi}^{(i)} = \operatorname{argmin}_{\boldsymbol{\psi}} \mathcal{R}(\boldsymbol{\psi}) + \frac{\rho}{2} \|\boldsymbol{\eta}^{(i)} - \boldsymbol{\psi} + \mathbf{u}^{(i-1)}\|_2^2 \quad (41b)$$

$$\mathbf{u}^{(i)} = \mathbf{u}^{(i-1)} + \boldsymbol{\eta}^{(i)} - \boldsymbol{\psi}^{(i)} \quad (41c)$$

for  $i = 1, 2, \dots$ . Note that, the two minimization problems in (41a) and (41b) can be efficiently solved as follows.

**Solving (41a).** For (41a), it is possible to show that:

$$\begin{aligned} \boldsymbol{\eta}^{(i)} &= \operatorname{argmin}_{\boldsymbol{\eta}} \frac{1}{2} \langle (\vec{\mathcal{Y}} - \mathcal{X} \boldsymbol{\eta}), \boldsymbol{\Sigma}^{-1} (\vec{\mathcal{Y}} - \mathcal{X} \boldsymbol{\eta}) \rangle + \frac{\rho}{2} \langle \boldsymbol{\eta} - \boldsymbol{\psi}^{(i-1)} + \mathbf{u}^{(i-1)}, \boldsymbol{\eta} - \boldsymbol{\psi}^{(i-1)} + \mathbf{u}^{(i-1)} \rangle \\ &= \operatorname{argmin}_{\boldsymbol{\eta}} -\frac{1}{2} \langle \boldsymbol{\eta}, \mathcal{X}^T \boldsymbol{\Sigma}^{-1} \vec{\mathcal{Y}} \rangle - \frac{1}{2} \langle \boldsymbol{\eta}, (\boldsymbol{\Sigma}^{-1} \mathcal{X})^T \vec{\mathcal{Y}} \rangle + \frac{1}{2} \langle \boldsymbol{\eta}, \mathcal{X}^T \boldsymbol{\Sigma}^{-1} \mathcal{X} \boldsymbol{\eta} \rangle \\ &\quad + \frac{\rho}{2} \langle \boldsymbol{\eta}, \boldsymbol{\eta} \rangle - \frac{1}{2} \langle \boldsymbol{\eta}, \boldsymbol{\psi}^{(i-1)} \rangle + \frac{1}{2} \langle \boldsymbol{\eta}, \mathbf{u}^{(i-1)} \rangle \\ &= \frac{1}{2} \langle \boldsymbol{\eta}, (\mathcal{X}^T \boldsymbol{\Sigma}^{-1} \mathcal{X} + \frac{\rho}{2} \mathbf{I}) \boldsymbol{\eta} \rangle + \langle \boldsymbol{\eta}, -\frac{1}{2} (\mathcal{X}^T \boldsymbol{\Sigma}^{-1} + (\boldsymbol{\Sigma}^{-1} \mathcal{X})^T) \vec{\mathcal{Y}} - \rho (\boldsymbol{\psi}^{(i-1)} - \mathbf{u}^{(i-1)}) \rangle \end{aligned} \quad (42)$$

where  $\langle \cdot, \cdot \rangle$  represents the inner product in a vector space.

Because the gradient vector of the right hand side of (42) can be obtained as

$$(\mathcal{X}^T \boldsymbol{\Sigma}^{-1} \mathcal{X} + \frac{\rho}{2} \mathbf{I}) \boldsymbol{\eta} - \frac{1}{2} (\mathcal{X}^T \boldsymbol{\Sigma}^{-1} + (\boldsymbol{\Sigma}^{-1} \mathcal{X})^T) \vec{\mathcal{Y}} - \rho (\boldsymbol{\psi}^{(i-1)} - \mathbf{u}^{(i-1)}), \quad (43)$$

we obtain the closed-form solution of (41a) by setting the gradient vector above to zero:

$$\boldsymbol{\eta}^{(i)} = (\mathcal{X}^T \boldsymbol{\Sigma}^{-1} \mathcal{X} + \frac{\rho}{2} \mathbf{I})^{-1} \left\{ \frac{1}{2} (\mathcal{X}^T \boldsymbol{\Sigma}^{-1} + (\boldsymbol{\Sigma}^{-1} \mathcal{X})^T) \vec{\mathcal{Y}} - \rho (\boldsymbol{\psi}^{(i-1)} - \mathbf{u}^{(i-1)}) \right\}. \quad (44)$$

**Solving (41b).** We re-write (41b) as

$$\begin{aligned} \boldsymbol{\psi}^{(i)} &= \operatorname{argmin}_{\boldsymbol{\psi}} \mathcal{R}(\boldsymbol{\psi}) + \frac{\rho}{2} \|\boldsymbol{\eta}^{(i)} - \boldsymbol{\psi} + \mathbf{u}^{(i-1)}\|_2^2 \\ &= \operatorname{argmin}_{\boldsymbol{\psi}} \lambda_1 \|\boldsymbol{\psi}\|_1 + \lambda_2 \|\mathbf{J} \boldsymbol{\psi}\|_2^2 + \frac{\rho}{2} \|\boldsymbol{\eta}^{(i)} - \boldsymbol{\psi} + \mathbf{u}^{(i-1)}\|_2^2 \quad . \\ &= \operatorname{argmin}_{\boldsymbol{\psi}} \lambda_1 \|\boldsymbol{\psi}\|_1 + \lambda_2 \langle \boldsymbol{\psi}, (\mathbf{J}^T \mathbf{J} + \frac{\rho}{2} \mathbf{I}) \boldsymbol{\psi} \rangle - \rho \langle \boldsymbol{\psi}, \mathbf{u}^{(i-1)} + \boldsymbol{\eta}^{(i)} \rangle \end{aligned} \quad (45)$$

The optimization problem (45) can again be solved numerically using ADMM. Converting (45) to a constrained problem yields:

$$\min_{\tilde{\boldsymbol{\psi}}, \boldsymbol{\theta}} \lambda_2 \langle \tilde{\boldsymbol{\psi}}, (\mathbf{J}^T \mathbf{J} + \frac{\rho}{2} \mathbf{I}) \tilde{\boldsymbol{\psi}} \rangle - \rho \langle \tilde{\boldsymbol{\psi}}, \mathbf{u}^{(i-1)} + \boldsymbol{\eta}^{(i)} \rangle + \lambda_1 \|\boldsymbol{\theta}\|_1, \quad \text{s.t. } \boldsymbol{\psi} = \boldsymbol{\theta}. \quad (46)$$

Then, for a given  $\omega > 0$ , the constrained problem is solved by repeating the following steps (for  $j = 1, 2, \dots$ ):

$$\begin{aligned} \tilde{\boldsymbol{\psi}}^{(j)} &= \operatorname{argmin}_{\tilde{\boldsymbol{\psi}}} \lambda_2 \langle \tilde{\boldsymbol{\psi}}, (\mathbf{J}^T \mathbf{J} + \frac{\rho}{2} \mathbf{I}) \tilde{\boldsymbol{\psi}} \rangle - \rho \langle \tilde{\boldsymbol{\psi}}, \tilde{\boldsymbol{\psi}} + \boldsymbol{\eta}^{(i)} \rangle + \frac{\omega}{2} \left\| \tilde{\boldsymbol{\psi}} - \boldsymbol{\theta}^{(j-1)} + \mathbf{v}^{(j-1)} \right\|_2^2 \\ &= \operatorname{argmin}_{\tilde{\boldsymbol{\psi}}} \frac{1}{2} \langle \tilde{\boldsymbol{\psi}}, 2\lambda_2 (\mathbf{J}^T \mathbf{J} + \frac{\rho + \omega}{2} \mathbf{I}) \tilde{\boldsymbol{\psi}} \rangle - \rho \langle \tilde{\boldsymbol{\psi}}, \mathbf{u}^{(i-1)} + \boldsymbol{\eta}^{(i)} + \omega \boldsymbol{\theta}^{(j-1)} - \omega \mathbf{v}^{(j-1)} \rangle \\ &= \frac{\rho}{2\lambda_2} (\mathbf{J}^T \mathbf{J} + \frac{\rho + \omega}{2} \mathbf{I})^{-1} (\mathbf{u}^{(i-1)} + \boldsymbol{\eta}^{(i)} + \omega \boldsymbol{\theta}^{(j-1)} - \omega \mathbf{v}^{(j-1)}), \end{aligned} \quad (47)$$

$$\begin{aligned} \boldsymbol{\theta}^{(j)} &= \operatorname{argmin}_{\boldsymbol{\theta}} \lambda_1 \|\boldsymbol{\theta}\|_1 + \frac{\omega}{2} \left\| \tilde{\boldsymbol{\psi}}^{(j)} - \boldsymbol{\theta} + \mathbf{v}^{(j-1)} \right\|_2^2 \\ &= S_{\lambda_1/\omega}(\tilde{\boldsymbol{\psi}}^{(j)} + \mathbf{v}^{(j-1)}) \end{aligned} \quad (48)$$

with  $S_{\lambda_1/\omega}(\cdot)$  being a soft-thresholding operator

$$S_{\lambda_1/\omega}(x) = \begin{cases} x - \lambda_1/\omega, & \text{if } x > \lambda_1/\omega \\ x + \lambda_1/\omega, & \text{if } x < -\lambda_1/\omega \\ 0, & \text{otherwise} \end{cases} \quad (49)$$

and  $\mathbf{v}^{(j)} = \mathbf{v}^{(j-1)} + \tilde{\boldsymbol{\psi}}^{(j)} - \boldsymbol{\theta}^{(j)}$ .

## 4. ADMM with Non-negativity Constraint

We show that the constrained problem (37) can be efficiently solved by modifying the ADMM algorithm described in Section 4. Firstly, we replace the inequality constraint in (37) with an equality constraint by introducing a penalty function and variable substitution:

$$\min_{\boldsymbol{\eta}} \frac{1}{2} (\vec{\mathcal{Y}} - \mathcal{X} \boldsymbol{\eta})^T \boldsymbol{\Sigma}^{-1} (\vec{\mathcal{Y}} - \mathcal{X} \boldsymbol{\eta}) + \mathcal{R}(\boldsymbol{\eta}) + \mathcal{I}(\tilde{\boldsymbol{\eta}}) \quad \text{s.t. } \mathcal{X} \boldsymbol{\eta} - \tilde{\boldsymbol{\eta}} = 0 \quad (50)$$

where  $\mathcal{I}(\tilde{\boldsymbol{\eta}}) = 0$  if  $\tilde{\boldsymbol{\eta}} \geq 0$ , and  $\mathcal{I}(\tilde{\boldsymbol{\eta}}) = \infty$  otherwise. Then, for  $\rho > 0$ , the scaled form of the

augmented Lagrangian of (50) is written as:

$$f(\boldsymbol{\eta}) + \mathcal{R}(\boldsymbol{\eta}) + \mathcal{I}(\tilde{\boldsymbol{\eta}}) + \frac{\rho}{2} \|\mathcal{X}\boldsymbol{\eta} - \tilde{\boldsymbol{\eta}} + \mathbf{u}\|_2^2 + \frac{\rho}{2} \|\mathbf{u}\|_2^2. \quad (51)$$

where  $f(\boldsymbol{\eta}) = \frac{1}{2}(\vec{\mathcal{Y}} - \mathcal{X}\boldsymbol{\eta})^T \boldsymbol{\Sigma}^{-1}(\vec{\mathcal{Y}} - \mathcal{X}\boldsymbol{\eta})$ .

Similar to (41), solving (51) using ADMM requires repeating the following iterations:

$$\boldsymbol{\eta}^{(i)} = \operatorname{argmin}_{\boldsymbol{\eta}} f(\boldsymbol{\eta}) + \mathcal{R}(\boldsymbol{\eta}) + \frac{\rho}{2} \|\mathcal{X}\boldsymbol{\eta} - \tilde{\boldsymbol{\eta}}^{(i-1)} + \mathbf{u}^{(i-1)}\|_2^2 \quad (52a)$$

$$\tilde{\boldsymbol{\eta}}^{(i)} = \max(0, \mathcal{X}\boldsymbol{\eta}^{(i)} + \mathbf{u}^{(i-1)}) \quad (52b)$$

$$\mathbf{u}^{(i)} = \mathbf{u}^{(i-1)} + \mathcal{X}\boldsymbol{\eta}^{(i)} - \tilde{\boldsymbol{\eta}}^{(i)} \quad (52c)$$

The evaluation of (56b) and (56c) are trivial, and the computational challenge lies in the minimization problem (68a). Fortunately, ADMM can again be used to solve (56a) by converting (56a) to a constrained problem:

$$\min_{\boldsymbol{\eta}} f(\boldsymbol{\eta}) + \mathcal{R}(\boldsymbol{\psi}) + \frac{\rho}{2} \|\mathcal{X}\boldsymbol{\psi} - \mathbf{c}\|_2^2, \quad \text{s.t. } \boldsymbol{\eta} = \boldsymbol{\psi} \quad (53)$$

where  $\mathbf{c} = \tilde{\boldsymbol{\eta}}^{(i-1)} - \mathbf{u}^{(i-1)}$ . Then, the ADMM for solving (53) involves the iterations:

$$\boldsymbol{\eta}^{(i)} = \operatorname{argmin}_{\boldsymbol{\eta}} f(\boldsymbol{\eta}) + \frac{\rho}{2} \|\boldsymbol{\eta} - \boldsymbol{\psi}^{(i-1)} + \mathbf{v}^{(i-1)}\|_2^2 \quad (54a)$$

$$\boldsymbol{\psi}^{(i)} = \operatorname{argmin}_{\boldsymbol{\psi}} \mathcal{R}(\boldsymbol{\psi}) + \frac{\rho}{2} \|\mathcal{X}\boldsymbol{\psi} - \mathbf{c}\|_2^2 + \frac{\rho}{2} \|\boldsymbol{\eta}^{(i)} - \boldsymbol{\psi} + \mathbf{v}^{(i-1)}\|_2^2 \quad (54b)$$

$$\mathbf{v}^{(i)} = \mathbf{v}^{(i-1)} + \boldsymbol{\eta}^{(i)} - \boldsymbol{\psi}^{(i)} \quad (54c)$$

A closer examination of (54) yields the following critical observations:

- (59a) takes exactly the same form of (46a) and the closed-form solution of (59a) is already given by (42).

- (59b) can be re-written as

$$\begin{aligned}
\boldsymbol{\psi}^{(i)} &= \operatorname{argmin}_{\boldsymbol{\psi}} \mathcal{R}(\boldsymbol{\psi}) + \frac{\rho}{2} \|\mathcal{X}\boldsymbol{\psi} - \mathbf{c}\|_2^2 + \frac{\rho}{2} \|\boldsymbol{\eta}^{(i)} - \boldsymbol{\psi} + \mathbf{v}^{(i-1)}\|_2^2 \\
&= \operatorname{argmin}_{\boldsymbol{\psi}} \lambda_1 \|\boldsymbol{\psi}\|_1 + \lambda_2 \|\mathbf{J}\boldsymbol{\psi}\|_2^2 + \frac{\rho}{2} \|\mathcal{X}\boldsymbol{\psi} - \mathbf{c}\|_2^2 + \frac{\rho}{2} \|\boldsymbol{\eta}^{(i)} - \boldsymbol{\psi} + \mathbf{v}^{(i-1)}\|_2^2 \\
&= \operatorname{argmin}_{\boldsymbol{\psi}} \lambda_1 \|\boldsymbol{\psi}\|_1 + \lambda_2 \langle \boldsymbol{\psi}, (\mathbf{J}^T \mathbf{J} + \frac{\rho}{2} \mathcal{X}^T \mathcal{X} + \frac{\rho}{2} \mathbf{I}) \boldsymbol{\psi} \rangle - \rho \langle \boldsymbol{\psi}, \mathcal{X} \mathbf{c} + \mathbf{u}^{(i-1)} + \boldsymbol{\eta}^{(i)} \rangle
\end{aligned} \tag{55}$$

which takes exactly the same form of (45), and can be solved following the same steps described from (46) to (49).

The discussions above show that the proposed inverse model can be extended to handle a linear inequality constraint (on the model output), which expands the applicability of the proposed model for a wider range of problems.

## 5. About the Computational Time of Problems P-I, P-II and P-III.

Although Problems P-I, P-II and P-III can be solved by the ADMM algorithm, it is noted that Problem P-I is formulated in the space-time domain, while Problems P-II and P-III are constructed in the spectral domain. As a result, the design matrix  $\mathcal{X}^{(P-I)}$  in (9) is a dense matrix, while the design matrices  $\mathcal{X}^{(P-II)}$  and  $\mathcal{X}^{(P-III)}$  in (20) and (31) are sparse (block diagonal), making the computation of  $\mathcal{X}^T \boldsymbol{\Sigma}^{-1} \mathcal{X}$ ,  $\mathcal{X}^T \boldsymbol{\Sigma}^{-1}$  and  $\boldsymbol{\Sigma}^{-1} \mathcal{X}$  faster in the ADMM algorithm. In addition, like many spectral methods, Problems P-II and P-III enable one to truncate the high-frequency components because each block of  $\mathcal{X}$ , in both (20) and (31), corresponds to a frequency level. This may help further reduce the computational time and is illustrated in Figure 12.

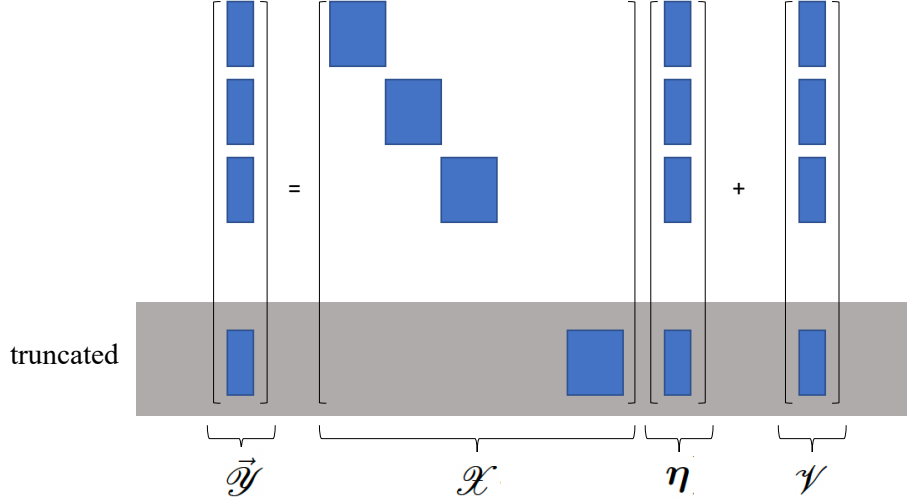


Figure 12: In problems P-II and P-III,  $\mathcal{X}$  is a block diagonal matrix with each block corresponding to a frequency, and it is possible to drop the blocks corresponding to high frequencies to further reduce the computational time.

## 6. Numerical Comparison on Different Choices of Regularizations

We compare the bias and MSE of the estimated initial condition  $\hat{\xi}(0, \mathbf{s})$  for different choices of regularizations, including

Approach 1). The proposed regularization

Approach 2). Generalized Lasso

Approach 3). Elastic Net

Approach 4).  $L_1$  regularization only

Approach 5).  $L_2$  regularization only

The comparison is based on Example-I presented in the paper. We repeated the “data simulation—statistical inference” process for 100 times, and compute the bias and MSE of the estimated initial condition  $\hat{\xi}(0, \mathbf{s})$ .



Figure (13) on the next page firstly shows the estimated initial condition using different regularizations. In particular, the 1st row of this figure shows the snapshots of the process at times 2, 5, 10, 15 and 20. The 2nd-6th rows of this figure show the contour plots of the estimated initial condition using the sensor observations up to times 2, 5, 10, 15 and 20. The thick blue level sets are respectively the 75th, 85th and 95th percentiles of the output generated by the inverse model, while the dashed thick level sets are the 50th and 60th percentiles.

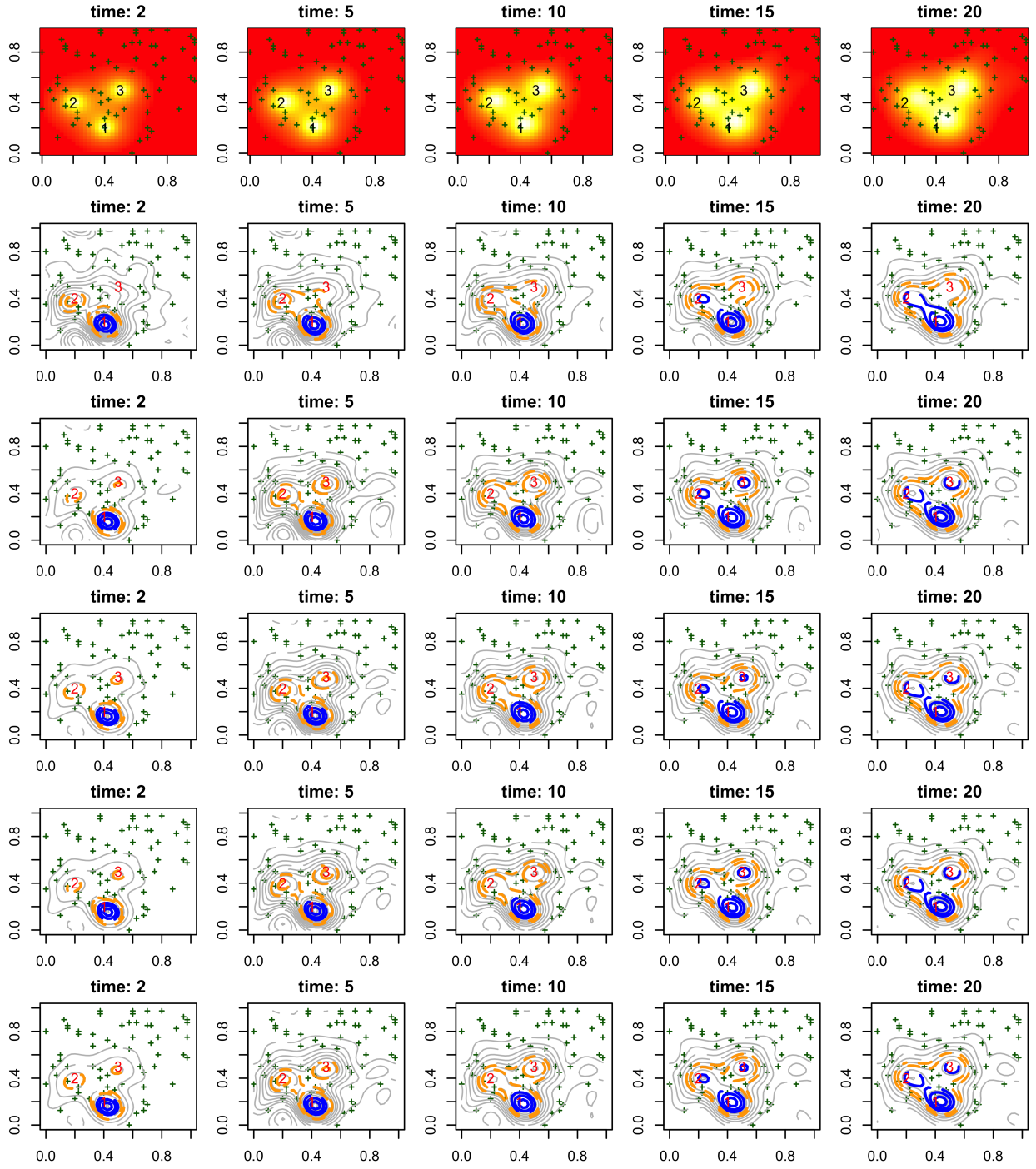


Figure 13: (1st row) snapshots of the advection-diffusion process at times 2, 5, 10, 15 and 20; (2nd-6th rows) estimated initial conditions at times 2, 5, 10, 15 and 20 using the proposed regularization (2nd row), Generalized Lasso (3rd row), Elastic Net (4th row),  $L_1$  regularization (5th row) and  $L_2$  regularization (6th row).

Next, Figure 14 shows the bias and MSE of the estimated initial condition for all choices of regularizations.

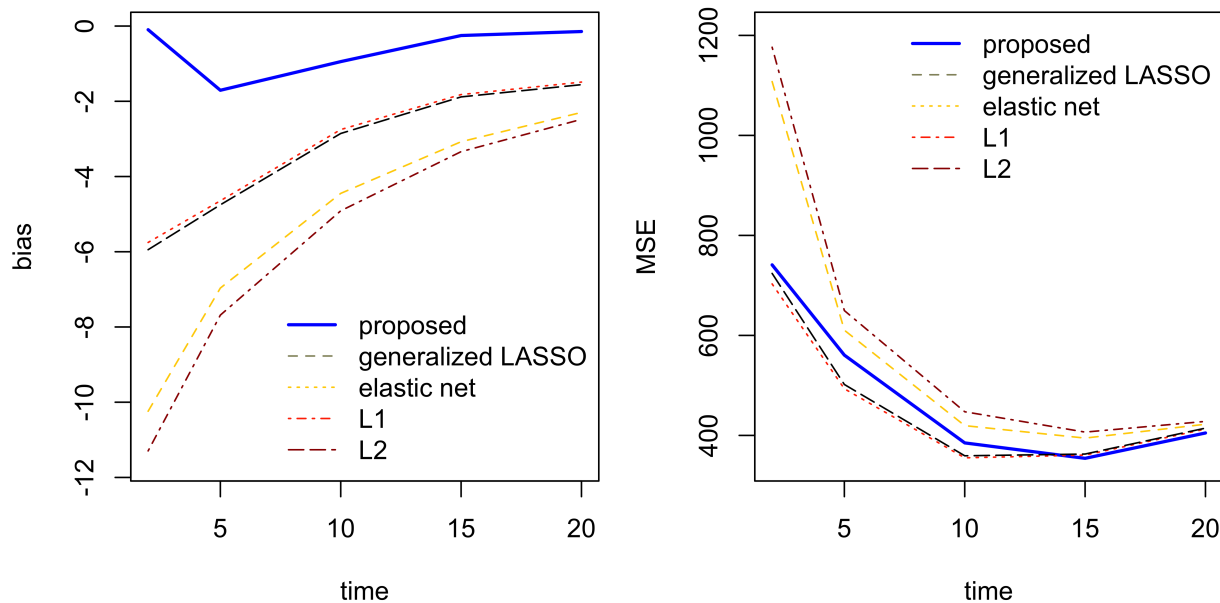


Figure 14: Bias and the Mean Squared Error (MSE) of the estimated initial conditions obtained based on different choices of regularizations.

It is seen that:

- ◇ The proposed regularization yields the lowest bias. The  $L_2$  regularization and the Elastic Net yield the highest bias, while the  $L_1$  regularization and the generalized Lasso yield similar performance.

- ◇ The proposed regularization yields a slightly higher MSE than the  $L_1$  regularization and generalized Lasso, while the  $L_2$  regularization and the Elastic Net yield higher MSE.

- ◇ During our investigation, we spent tremendous amount of time on experimenting on different choices and combinations of how regularizations can be added. One challenge that we found was that the estimated spectral coefficients in  $\boldsymbol{\eta}$  may dramatically vary from one frequency to another (for example, we may see a sudden spike of the coefficient corresponding to a higher frequency). However, because this paper focuses on the estimation of smooth initial condition, ideally the spectral coefficients should gradually decay as the frequency

increases (not necessarily monotone). Adding an  $L_1$  or  $L_2$  regularization alone does not automatically overcome this difficulty, although it promotes sparsity. Hence, we modified the Fused Lasso and added a second regularization which helps to impose the “smoothness among the components in corresponding to adjacent frequencies” (to prevent the neighboring spectral coefficients from varying dramatically). As a result, we may see the gradual decay of the estimated spectral coefficients that give rise to a smooth initial conditions.